A Unique Set of Transition Matrix Elements for the $^2\mathrm{H}(\vec{d},\gamma)^4\mathrm{He}$ Reaction at $E_{beam} = 115$ keV

by

Konstantin Sabourov

Department of Physics
Duke University

Date

Approved:

Henry R. Weller, Supervisor

Shailesh Chandrasekharan

Henry Greenside

Calvin Howell

Stephen Teitsworth

Dissertation submitted in partial fulfillment of
the requirements for the degree of
Doctor of Philosophy in the Department of
Physics in the Graduate School
of Duke University

2003

Abstract

(Physics – TUNL)

A Unique Set of Transition Matrix Elements for the $^2\mathrm{H}(\vec{d},\gamma)^4\mathrm{He}$ Reaction at $E_{beam} = 115$ keV

by

Konstantin Sabourov

Department of Physics
Duke University

Date

Approved:

Henry R. Weller, Supervisor

Shailesh Chandrasekharan

Henry Greenside

Calvin Howell

Stephen Teitsworth

An abstract of a dissertation submitted in partial fulfillment of the requirements for the degree of Doctor of Philosophy in the Department of Physics in the Graduate School of Duke University

2003

Abstract

A Unique Set of Transition Matrix Elements for the ^{2}H$(\vec{d},\gamma)^4$He Reaction at $E_{beam} = 115$ keV.

The synthesis of the light elements in the first thousand seconds of the evolution of the Universe can be used to test the standard cosmology. Big-Bang Nucleosynthesis (BBN) is the only observational test of the hot big-bang model at early times, and the comparison between the calculated and observed abundances of ^{2}H, ^{3}He, ^{4}He, and ^{7}Li can be used to constrain the predicted baryon density of the Universe as well as the number of species of light particles. To reliably calculate the light element abundances it is necessary to reduce uncertainties in the BBN network reaction rates. The deuteron-deuteron radiative capture reaction is one of the deuterium-burning processes for which the cross section is not known well at very low energies (10–100 keV). Polarized beams allow accurate extraction of the complex transition matrix elements (TMEs) from the measured analyzing powers, such studies of the reaction mechanisms should lead to a reliable extrapolation of the cross section to energies relevant to BBN.

Prior to any polarized beam measurements, the ^{2}H(d, γ)^{4}He reaction was believed

to proceed entirely via electric quadrupole (E2) radiation at very low energies, a result of s-wave (angular momentum of the two deuterons l=0) capture. However, low-energy measurements of ^{2}H($\vec{d},\gamma$)^{4}He analyzing powers revealed the presence of non-E2 radiation, appearing because of the presence of other than s-wave capture terms. Those studies showed that 50 to 85% of the total capture strength is due to p-wave (l=1) capture. Unfortunately, the data analysis did not allow an unambiguous set of TMEs to be extracted, so that a critical test of theoretical results could not be performed.

In my work we were able to reduce uncertainties and expand the angular range in the measurements of the polarization observables. We obtained angular distributions for vector and tensor analyzing powers A_y and T_{20} by stopping a polarized deuteron beam of E_d(lab)=115 keV in a heavy-water ice target. The analysis of the data included l=1 partial waves in addition to the s-wave (E2) capture term, corresponding to electric dipole (E1) and magnetic quadrupole (M2) radiation. A unique fit was obtained with an s-wave (E2) capture strength of 55±8% of the total strength, and a p-wave strength of 29±6% (E1) and 16±3% (M2), for a total of 45±7%. The measured analyzing powers and the results of the TME analysis were compared to refined resonating-group-model calculations. The observed and the calculated transition amplitudes were found to be in good agreement, although the p-wave phases disagree with the experimentally determined results, which will require further comparison of our analysis with the calculation.

Finally, the p-wave strength established by this work leads to the extrapolated value of the astrophysical S-factor for the ^{2}H($\vec{d},\gamma$)^{4}He reaction of 2 times lower than the previous best calculation.

Acknowledgements

None of this work would be possible without help of all the members of Radiative Capture group and our favorite TUNL technicians. Henry Weller provided guidance in every aspect of my research. The post-docs, John "Ned" Kelley, Sally Gaff, Anton Tonchev, and Mohammad Ahmed taught me a lot of real-life physics. John Dunham, Richard O'Quinn, Paul Carter, and Sid Edwards made all the things in the lab working, despite everything. Help from Richard Prior and Mark Spraker, Nasser Kalantar and Kara Keeter (with special thanks) cannot be underestimated.

The very special thank you is to fellow grad students. Erics, Wulf and Schreiber, and Shane Canon were always fun to be around, and so patient to answer my various questions. The design and getting of $^{2}\mathrm{H}(\vec{d},\gamma)^{4}\mathrm{He}$ up and running would not be possible without all the long hours and effort from SteveO Nelson. Brendan Crowley, Kaveri Joshi: guys, you've made a great decision, and it was the best time with you hanging around. Brent Perdue, good luck. Rob and Shige, we had some great time.

Of course, it all started making sense only as I met Amanda. Thank you for making it all happen.

I would like to thank my parents, on both sides of the ocean, for help in making the right choices, your patience, and support.

Contents

Abstract **iv**

Acknowledgements **vi**

List of Figures **ix**

List of Tables **xiii**

1 Introduction **1**

1.1 Few-Body Nuclear Reactions 1

1.2 Review of Experimental Data and Theoretical Efforts 5

1.3 Overview of the present work 13

2 Experimental Setup and Methods **15**

2.1 Polarized Beam 15

2.1.1 Beam Polarization 17

2.1.2 Polarized Ion Source 20

2.1.3 Polarimetry 25

2.2 Beam Transport and Target 29

2.3 NaI(Tl) Detectors 35

2.3.1 Physics of γ-ray-detection 35

2.3.2 Detector Design 39

2.4 Electronics 42

2.5 Data Acquisition 47

3 Polarization Observables **49**
3.1 Analyzing Powers As Asymmetries 49
3.2 Channel Spin Coupling Scheme 56
3.3 Transitions Involved in the Reaction 58
3.4 From Angular Distributions to TMEs 62

4 Data Analysis **64**
4.1 Sorting 64
4.2 Data Analysis Software 65
4.3 Spectra Fitting 65
4.4 Errors and Corrections 70
4.5 Observed Angular Distributions of Analyzing Powers 72

5 TME Analysis **80**

6 Results and Discussion **86**
6.1 Direct Capture Model 86
6.2 Resonating Group Model 89
6.3 Comparison of Data with Models 92

7 Conclusion **97**

Bibliography **100**

Biography **103**

List of Figures

1.1 Energy dependence of ^{2}H(d,γ)^{4}He total cross section. The experimental data are from [Zur63], [Mey69], [Deg92], [Wil85], [Wel86], [Bar87], and [Kra92]. The results of pure E2 semi-microscopic calculations [Ass87] are presented as well (solid line). Dashed line is the s-wave capture to the D-state of ^{4}He, dash-dotted is the d-wave capture to the S-state, and the dotted line is the d-wave capture to the D-state. The d-wave to the S-state capture is dominant at energies above 1 MeV, while the s-wave capture is important at low energies. It has been found that significant non-E2 contribution is present below 1 MeV. 7

1.2 Energy dependence of ^{2}H(d,γ)^{4}He astrophysical S-factor. The experimental data are from [Zur63], [Mey69], [Deg92], [Wil85], [Wel86], [Bar87], and [Kra92]. The results of pure E2 semi-microscopic calculations [Ass87] are presented as well (solid line). Dashed line the is s-wave capture to the D-state of ^{4}He, dash-dotted is the d-wave capture to the S-state, and the dotted line is the d-wave capture to the D-state. 11

2.1 Experimental setup. Tensor-polarized deuterons are accelerated down the LECAP beam-line onto a frozen heavy-water target. The target chamber is biased to negative 35 kV and isolated from the detectors with plastic. The NaI(Tl) detectors are placed inside anti-coincidence shields. Passive shielding is set up to reduce the neutron flux into the detectors. 16

2.2 Coordinate system used to describe analyzing powers according to Madison Convention [Bar71] 19

2.3 Schematic drawing of the atomic beam polarized-ion source. The hydrogen or deuterium gas is supplied into the dissociator on the left side of the figure. The gas atoms pass through the series of magnetic field and rf-transition regions, are ionized in the ECR cavity, and exit the source through the Wien filter. 21

2.4 The Breit-Rabi diagram for deuterons. The sextupole magnets filter out the atoms with $mj = -1/2$ (states 4, 5, and 6). The RF transition units produce population differences of the states 1, 2, and 3, thus creating nuclear polarization of the deuteron beam 23

2.5 The side view of the target chamber. The vapor line can be rotated to face the cold target plate for ice-target production. In this position the tuning target can be used to measure the beam current. During data-taking the tuning target and the vapor line are rotated out of the beam. 30

2.6 Side view of the biased target chamber setup. The chamber was supported by the liquid nitrogen dewar, which bottom was resting on the plastic high voltage shielding. The valves were closed during evaporation of heavy water onto the cold target plate. The use of non-conductive plastic tubes allowed us to place the pump and the silicon detector at ground potential. 32

2.7 A typical spectrum produced by the silicon detector. The threshold is set below the 2.7 MeV proton peak. The presented spectrum is for one-hour run and corresponds to proton counting rate of 40 Hz. . . . 33

2.8 An example of using the silicon detector for target quality monitoring. When the monitor detector count rate started to drop, a new ice target was made (shown by the arrows). 34

2.9 Calibration spectrum for a NaI(Tl) detector with an Am-Be source. The major source line is 4.4 MeV, result of de-excitation of ^{12}C produced in α-capture on ^{9}Be. The first escape peak at 3.9 MeV is also visible. The 6.8 MeV peak is due to the radiative capture of neutrons on iodine of the crystal. The two visible natural background peaks are the 2.2 MeV line (radiative capture of thermal neuterons on protons) and the 2.6 MeV line of ^{226}Th. 37

2.10 γ-ray interaction with NaI crystal. At low energies photo-electric effect (dotted line) and scattering (dashed line) dominate, while at energies above 10 MeV most of the γ-ray energy is deposited through the pair-production (dash-dotted line) The total cross section is shown with the solid line. 38

2.11 Energy spectra produced from a NaI(Tl) detector. Both are results of week-long measurement. The top one is the raw signal, everything that is seen by the detector. The bottom one is produced by vetoing cosmic-ray induced events in the raw spectrum. 41

2.12 The electronics diagram for the NaI(Tl) detector. Utilization of pulse shaping with the clipping line and TFA, and fast linear gate setup, helps to reduce pile-up in spectra. A copy of the discriminator output is tested for coinsidence with the plastic shield detector. In event of considence the cosmic-ray veto bit is set to reject the event. 43

2.13 The electronics diagram for the silicon solid-state detector 47

3.1 Rotation of the "internal" coordinate system $\xi\eta\zeta$ into the system of the Madison Convention xyz. The first Euler angle is 0°, the ζ-axis being the *vertical*. The second rotation is around the *line of nodes*, the η-axis, by -β°; it is negative, because the rotation is from ξ-axis to ζ-axis. It brings the ξ-axis in the x-y plane, the position shown as α. The final rotation is around the ζ-axis, the *figure axis*, which positions the η-axis along the y-axis. The corresponding angle is -(90-ϕ)°, again negative, because the rotation is clockwise in the ξ-ζ plane. 51

3.2 Electromagnetic transitions from scattering states of two deuterons to the ground state of ^{4}He. The alpha-particle ground state, $J^\pi = 0^+$, T=0, is considered as combination of dominating $^1S_0$ (L=0, S=0) state with $^5D_0$ (L=2, S=2) state admixture. The spin-isospin selection rules help us in estimation of the relative transition strength. 60

4.1 NaI(Tl) detector response function used for spectra fitting. The functional expression is given in the text. The parameter values are in the Table 4.1 68

4.2 A typical spectrum used to obtain the capture γ-ray-yields. The NaI(Tl) detector line-shape (shown in Figure 4.1) and the background function (given by Equation 4.1) are fitted simultaneously. The yield is calculated as the difference of the total fit (line-shape and the background, solid curve) and the background (dashed curve). 69

4.3 Data points for $A_y(\theta)$ and $T_{20}(\theta)$ beam energy of E_d=115keV. 75

4.4 Data points from the previous measurements of $^2H(\vec{d},\gamma)^4He$ reaction at E_d=80keV(differential cross section, A_y and A_{yy}). Our measurement expand the data set for this energy by including T_{20}. 76

5.1 Data points and the TMEFIT results for E_d=80keV. The differential cross section, $A_y(\theta)$ and $A_{yy}(\theta)$ are from previous experiment [Kra92]. Inclusion of $T_{20}(\theta)$ data resulted in only two solutions. 82

5.2 Data points and the TMEFIT results for E_d=115keV. The analysis produced a unique solution for the transition matrix elements. 84

6.1 Measured vector analyzing power $A_y(\theta)$, corrected for finite geometry, the TMEFIT results (solid curve) , and the refined resonating group calculation results (dashed curve) for $< E_d >_{cm}$=46keV. 94

6.2 Measured tensor analyzing power $T_{20}(\theta)$, corrected for finite geometry, the TMEFIT results (solid curve), and the refined resonating group calculation results (dashed curve) for $< E_d >_{cm}$=46keV. 95

7.1 Energy dependence of $^2H(d,\gamma)^4He$ astrophysical S-factor. The experimental data are from [Zur63], [Mey69], [Deg92], [Wil85], [Wel86], [Bar87], and [Kra92]. The pure E2 semimicroscopic calculation (solid curve) and the refined resonating group calculation (the lower solid line for energies below 60 keV) are shown. To directly compare the two, the RRGM calculation is scaled up by factor of 1.6. Inclusion of the p-wave capture changes the slope of the S-factor at low energies. . . 99

List of Tables

2.1 SFP measurements during December 2000 A_y run. 28

2.2 Nuclear polarimeter measurements during December 2000 A_y run. The yields were obtained during three measurements with unpolarized and two polarized states. The total charge on the target in each spin state was equal. 29

4.1 NaI(Tl) detector response function fit parameters. The corresponding line-shape is shown in the Figure 4.1. The high precision of the response function coefficients is necessary to obtain finite values of the response function. 67

4.2 Data for $A_y(\theta)$, E_d=115keV. The asymmetry $(Y_1 - Y_2)$ for the 132°point has different sign, because the detector was placed to the right from the target. 73

4.3 Data for $T_{20}(\theta)$, E_d=115keV. 73

4.4 Data for $T_{20}(\theta)$, E_d=80keV. 73

4.5 Finite geometry corrected data for E_d=115keV. 77

4.6 Parameters for the stopping power of hydrogen in oxygen. The functional form of $STP(E)$ is given by Equations 4.9 and 4.10. 78

5.1 Results of TMEFIT for E_d=80 keV. 81

5.2 Results of TMEFIT for E_d=115 keV. 83

6.1 Results of the TME fit analysis and RRGM calculations for $< E_d >_{cm}$=46 keV. The rest of the calculated capture strength (4%) is due to d-wave E2 capture, which was not included in the TME fit. The calculated phases, shifted by -122° for comparison with the TME analysis are shown in parentheses. 93

Chapter 1

Introduction

1.1 Few-Body Nuclear Reactions

The phrase "precision cosmology" is becoming a valid description of modern models of the early Universe. The results inferred from the predictions of Big-Bang Nucleosynthesis (BBN) , combined with the latest Cosmic Microwave Background (CMB) anisotropy measurements, give independent and accurate predictions of the baryon density and can be used to test the standard cosmology framework [Kap01]. The abundances of the light nuclei, ^{2}H, ^{3}He, ^{4}He, and ^{7}Li have been used to test the consistency of the hot big-bang model at early (first 10^3 seconds) stages of evolution of the Universe. To construct the BBN reaction network, the astronomical measurements of the light element abundances need to be complemented by the reaction rate knowledge in the relevant energy region (from few tens to few hundreds of keV). The deuteron-deuteron radiative capture reaction is one of the deuterium-burning processes for which the cross section is not well known at very low energies. The studies

of nuclear reactions, such as the one presented in this work, lead to a better understanding of how these reactions proceed at very low energies. The experimental data can be used to test theoretical models, which consequently provide the reaction cross sections at the astrophysically important energies (the region impractical for direct laboratory measurements due to extremely low reaction rates). Through these models these data also test and refine out knowledge of the nucleon-nucleon interactions since these lie at the base of these models.

Few-body systems are excellent test subjects for our understanding of nucleon-nucleon interactions. Simple systems can be sensitive to various parts of the interaction: the deuteron properties are defined by the tensor component of the two-nucleon (NN) force, and the triton binding energy cannot be calculated without taking the three-body (3N) forces into account. While some properties of light nuclei and some reaction observables can be described in relatively simple terms, some observables require detailed knowledge of the nuclear interaction. To illustrate this, let us consider the relation between reaction observables and transition matrix elements. A nuclear reaction can be described via transition matrix elements (TMEs), which are determined by the wave functions of the projectile and target, the wave functions of the reaction products, and the interaction Hamiltonian. In general, TMEs are complex variables, possessing amplitudes and phases. The number of TMEs needed to describe a reaction depends on the number of reaction channels and the nature of the interaction. Since the polarization observables are the result of interference effects, even small matrix elements involved in the reaction can be deduced. For this reason, simple models of the wave functions and the interaction might suffice to describe the cross section, but a correct calculation of the analyzing powers is typically more challenging.

A well known example of difficulties with analyzing powers is the "A_y puzzle" [Koi87]. This term refers to the inability of full three-body calculations to reproduce the nucleon-deuteron scattering vector analyzing power A_y. While the cross section and some of the tensor analyzing powers can be calculated correctly, the experimental values of $A_y(\theta)$ are in disagreement with the calculations. It is believed that a potential utilizing both NN and 3N forces in a fully consistent way may be able to solve this problem.

From the same point of view, we can see how analyzing power measurements can help in improving the models and expanding our knowledge of nuclear reaction mechanisms. Experiments utilizing polarized beams can provide such details about the reaction, details that could not be inferred from unpolarized beam experiments or that would require extremely high precision differential cross section measurements.

The Radiative Capture group of TUNL has performed a number of capture experiments on light nuclei at low energies. Use of polarized proton and deuteron beams made it possible to perform a transition matrix element analysis on the obtained angular distributions of vector and tensor analyzing powers. As a continuation of the effort to provide experimental data for low-energy radiative capture reactions, we have in this work performed measurements of polarization observables for the $^2\mathrm{H}(\vec{d},\gamma)^4\mathrm{He}$ reaction at deuteron energies of 115–0 keV.

The $^2\mathrm{H}(\vec{d},\gamma)^4\mathrm{He}$ reaction is of particular interest because of the symmetry in the entrance channel resulting in a simpler set of TMEs. The symmetry condition of the total wave function for identical bosons requires that the sum of the relative angular momentum and the total spin, $l+s$, for the deuterons should be even. This limits the number of partial waves to be considered. Furthermore, we can investigate the types of radiation that can be emitted and evaluate which transitions should be

taken into account. The details of the present TME evaluation will be given in Section 3.3, but we can make a short argument here. The ^{4}He ground state ($J^\pi = 0^+$) can be considered as a superposition of the S-state (angular momentum L=0 and spin S=0) and the D-state (L=2, S=2) in the d-d cluster model. In this picture, the D-state admixture arising from the L=2 motion of the two deuterons is small, 4–7%, but its presence enables more partial waves to participate in the capture reaction. Considering electromagnetic radiation with multipolarity less than 2, the following transitions are allowed: (E1, $^3p_1$), (M1, $^5d_1$), (E2, $^1d_2$), (E2, $^5s_2$), (E2, $^5d_2$), (E2, $^5g_2$), (M2, $^3p_2$), (M2, $^3f_2$) (using the notation $^{2s+1}l_j$, where l, s, and j are relative orbital angular momentum, total spin, and total angular momentum of the two deuterons in the entrance channel, respectively). Since $\Delta s = 0, \pm 1$ for all of these transitions, all of the $s = 2$ continuum states will be captured into the D-state of ^{4}He. The singlet E2 d-wave is captured into the predominant S-state. The triplet p-waves can be captured to either state, but they involve either spin-flip E1 or M2 radiation, and would be expected to be suppressed in comparison to $\Delta s = 0$ transitions. The E1 radiation is even more suppressed by the isospin selection rule ($\Delta T = \pm 1$ in self-conjugate nuclei).

If the deuterons are mostly captured into the S-state of the alpha particle, the E2 d-wave should be the dominant transition. At low energies one would expect the E2 s-wave capture to the D-state to become the strongest because the d-waves are suppressed by penetrability through the Coulomb-centrifugal barrier. The experimental data does confirm these expectations: above 1 MeV the cross section can be described by pure d-wave E2 capture to the S-state of ^{4}He, and at lower energies there is an increase in the total cross section with respect to pure d-wave capture caused by capture to the D-state.

The analysis of the early cross section measurements included only E2 transitions. However, the measurements of polarization observables, such as vector and tensor analyzing powers, in addition to the differential cross section, proved that there is a significant non-E2 contribution below E_d=1 MeV. The transition matrix element analysis of the low-energy data at E_d=80 keV showed a surprisingly strong p-wave capture contribution. While the previous work was unable to produce a unique solutions at very low energies, it is the intention of the present investigation to attempt just that.

The knowledge of the reaction mechanism greatly affected the extrapolated value of the ^{2}H(d, γ)^{4}He reaction cross section. The discovery of the D-state admixture in the ^{4}He ground state [Wel84], and the analysis of the differential cross section data taking the s-wave capture into account, resulted in value of the extrapolated astrophysical S-factor (this quantity, related to the absolute cross section will be discussed later) of 32 times higher than the previously estimated [Bar87]. The experimental evidence for the p-wave capture results in reevaluation of the extrapolated cross section again.

In the next section we will give a review of experimental and theoretical analysis of the ^{2}H(d, γ)^{4}He reaction, then focus on our present work.

1.2 Review of Experimental Data and Theoretical Efforts

As mentioned above, the measurements of the ^{2}H(d, γ)^{4}He reaction cross section at energies above 1 MeV [Mey69], [Wel86] were in agreement with the assumption

of predominant E2 d-wave capture into the L=0, S=0 component of the ^{4}He ground state. Simple direct capture calculations were sufficient to describe the data. However, the lack of data at low energies did not permit a reliable extrapolation of the cross section to the astrophysically important energies in the region of keV.

The presence of the D-state component in the ^{4}He ground state was established by $T_{20}(\theta)$ measurements at E_d=9.7 MeV [Wel84]. The non-zero value of this tensor analyzing power is primarily a result of interference between the transition matrix elements of capture to the S- and D-states of the alpha particle. The existence of the D-state allowed the additional TMEs, corresponding to E2 transitions, to be considered in the capture: the quintet s-, d-, and g-waves.

At low energies the s-wave transition was assumed to prevail because higher angular momenta partial-wave amplitudes would be suppressed by the centrifugal barrier. The early measurements of the differential cross section at energies below E_d=500 keV [Wil85] and [Bar87] showed an increase in the absolute cross section above earlier predictions. The increase was believed to be due to the presence of the s-wave capture to the D-state of ^{4}He.

The experimental data were used to obtain the amount of D-state admixture in the alpha particle ground state. Several direct capture and microscopic studies of the reaction were able to reproduce the cross section data [Kad86], [Ass87], [Bar87],[Wel86], [Pie87], and [Blü87]. All of the studies assumed pure E2 radiation. It was found that tensor force effects between and in the deuterons and in ^{4}He can play an important role in extraction of the D-state probability.

Analyzing power measurements allowed for a more extensive transition matrix element analysis. The analysis of polarization observables (tensor and vector analyzing powers) at E_d=10 MeV [Mel86] showed that up to 15% of the cross section

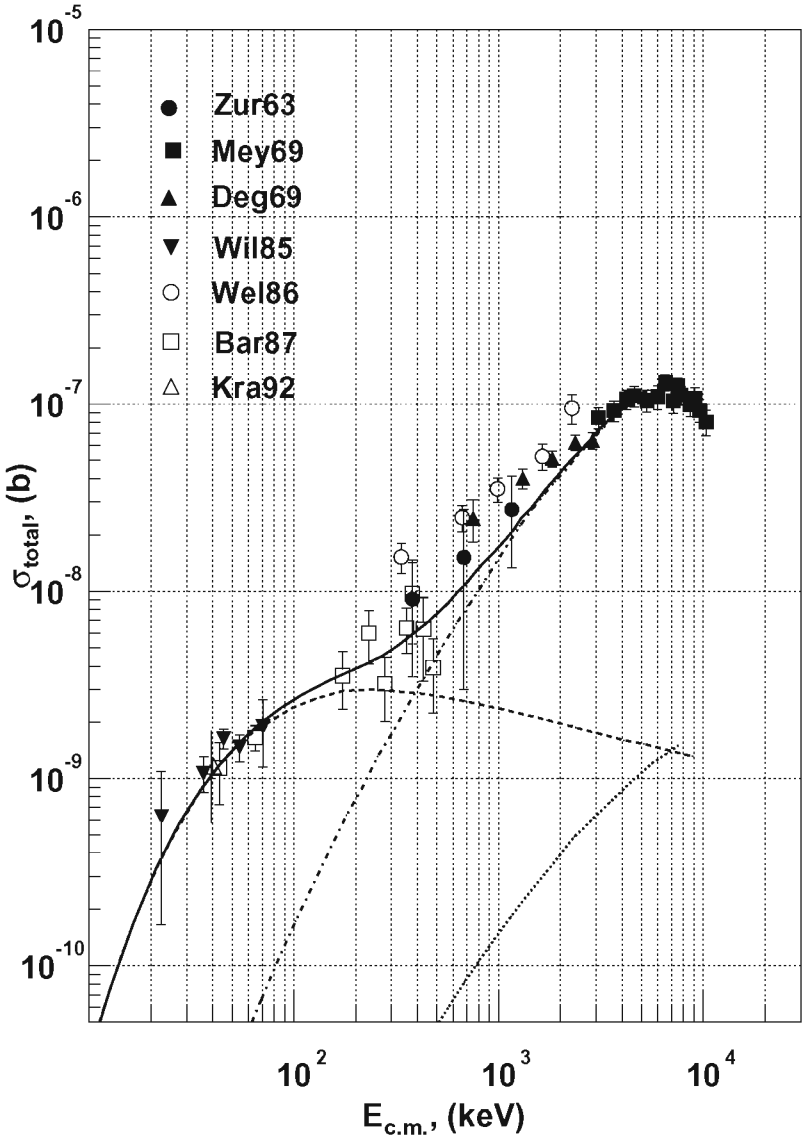

Figure 1.1: Energy dependence of ^{2}H(d, γ)^{4}He total cross section. The experimental data are from [Zur63], [Mey69], [Deg92], [Wil85], [Wel86], [Bar87], and [Kra92]. The results of pure E2 semi-microscopic calculations [Ass87] are presented as well (solid line). Dashed line is the s-wave capture to the D-state of ^{4}He, dash-dotted is the d-wave capture to the S-state, and the dotted line is the d-wave capture to the D-state. The d-wave to the S-state capture is dominant at energies above 1 MeV, while the s-wave capture is important at low energies. It has been found that significant non-E2 contribution is present below 1 MeV.

involves processes in which the tensor force plays a role, either in the entrance or exit channel. Therefore, the reaction cannot be used to determine the D-state admixture in the ^{4}He wave function unless the D-state of the deuteron and other tensor-force effects are taken into account.

Further measurement of the analyzing powers [Lan88] and [Lan89] at energies from 1 to 15 MeV showed a significant non-E2 contribution (with almost equal E2, E1, and M2 components for E_d=1.2 MeV[Lan88]).

More calculations on the ^{2}H$(\vec{d},\gamma)^4$He reaction, taking into account the measured polarization observables and based on the potential [Blü87] and microscopic multi-channel resonating group models [Wac87], [Arr88], and [Arr91], still considered the E2 transition as dominant. The calculations showed qualitative agreement with the data and confirmed the importance of the complete knowledge of the entrance channel wave functions.

The polarization observables measurements in the low-energy region, 80 0 keV [Kra92] and [Kra93], demonstrated a significant p-wave admixture in the continuum wave functions. The analysis of the differential cross section, A_y, and A_{yy} data showed that pure s-wave E2 transitions cannot describe the polarization observables. The transition matrix element analysis showed that 50% to 85% of the total capture strength arose from p-wave (E1/M2) capture. Direct capture and microscopic coupled-channel resonating group model calculations only qualitatively described the data but certainly indicated the p-wave presence and the importance of the tensor force, and the coupling of the p-T, n-^{3}He and the d-d channels.

Extensive measurements of analyzing powers were done at E_d=20, 30, and 50 MeV [Whi93]. This energy region was chosen to simplify the analysis: above E_d=15 MeV the p-wave capture is negligible, and below 95 MeV the long wavelength ap-

proximation is still valid. The angular distributions of the differential cross section, A_y, A_{yy}, and T_{20} were analyzed to extract the two-deuteron D-state component and the transition matrix elements involved in the reaction. Direct capture and microscopic coupled-channel resonating group model calculations with realistic NN potentials yielded fairly good agreement with the data. It was concluded that more extensive calculations, including more reaction channels and more precise potentials, would provide a better description of the data in this energy region as well as at lower energies.

The improved NN potentials and microscopic models led to a more successful description of light nuclei. In-depth comparison of R-matrix and resonating group model calculations at E_d=6 MeV for various d-^{2}H, p-^{3}H, and n-^{3}He data [Hof97] showed that the use of a modern, realistic nucleon-nucleon force is very promising in explaining the data. The potentials with a strong tensor-force component (like Argonne V14 or V18) and three-body terms are expected to produce the best results.

The increase in computing power and availability of new algorithms allowed for calculations of wave functions for a variety of light nuclei [Wur97]. The calculations, based on the refined resonating group method and using an effective NN potential, were aimed to treat the stable nuclei ^{4,6,8}He and unstable systems ^{5,7}He on the same footing. It was possible to reproduce the wave functions and energy spectra of light nuclei, but for heavier elements one would need to adjust the effective NN potential.

Considerable effort has been put into the development of accurate NN potentials, as well as into the formulation of 3N forces and the role of four-nucleon interactions. One of the most advanced NN potentials to date is Argonne V18 [Wir95]. This non-relativistic potential is based on fits to *pp* and *np* scattering data (taken directly from Nijmegen NN scattering database), as well as to low-energy *nn* scattering parameters

(singlet nn scattering length) and the deuteron binding energy. As a result, the charge-independence breaking is explicitly taken into account.

Presently there is no 3N force model that works with all NN potentials: for each NN model the parameters in a 3N potential must be adjusted to produce the correct three-body binding energies and wave functions. Two of the most common 3N models used to augment the NN potentials are the Tucson-Melbourne [Coo79] and the Urbana-IX [Pud97].

As discussed in the recent study of the alpha-particle structure based on the modern nuclear forces [Nog02], the few-body bound states can provide invaluable information about the nature of 3N forces. This study considered the NN potential model dependences and evaluated the magnitude of four-body interactions (found to be considerably much smaller than 3N forces). The experimental data on few-body bound states are also necessary for development of 3N interaction models consistent with NN forces [Bed00].

Recent calculations of the ^{4}He scattering system [Hof02] based on the resonating group model were used to investigate the effects of 3N forces. The study employed realistic NN and 3N potentials, including additional 3N terms [Can00]. The 3N forces have great impact on the phase shifts, the cross section, and the analyzing powers. A comparison with the R-matrix analysis can help determine the operator structure of the 3N forces. Inclusion of high enough partial waves in the calculation (which is rather straightforward but very computationally intensive) should result in accurate predictions for the analyzing powers.

A detailed knowledge of the reaction mechanism, such as the energy dependence of amplitudes and phases of the reaction matrix elements, would allow a precise extrapolation of the reaction cross section to the energies relevant to astrophysics,

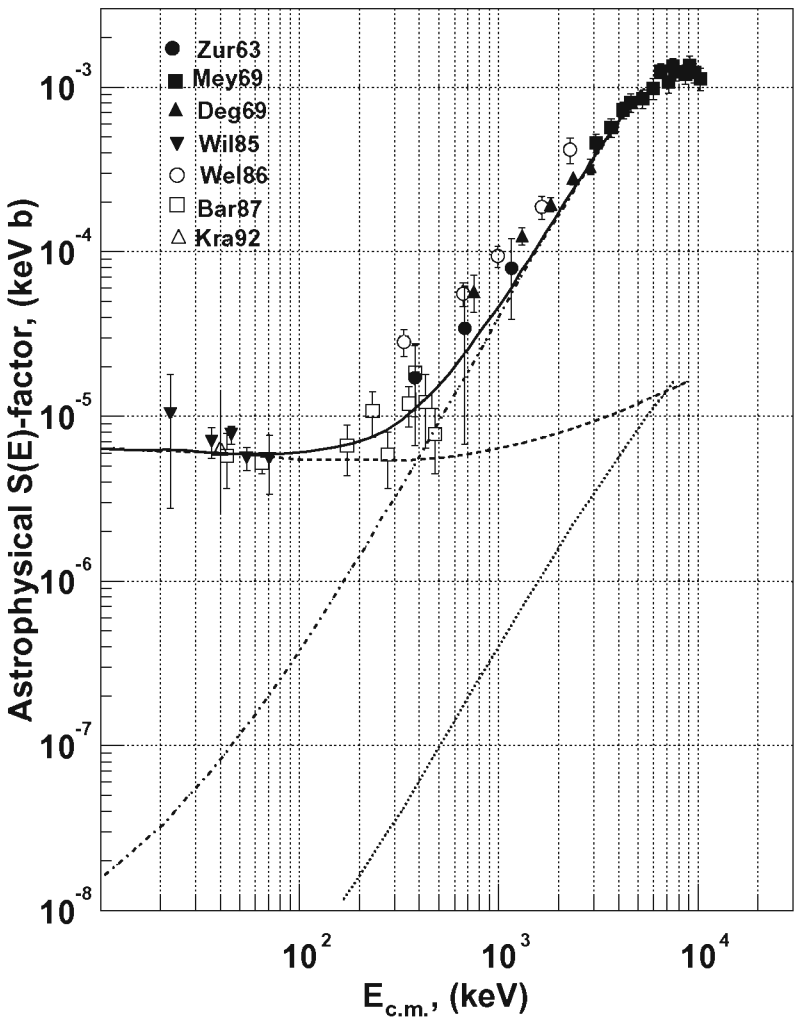

Figure 1.2: Energy dependence of ^{2}H(d, γ)^{4}He astrophysical S-factor. The experimental data are from [Zur63], [Mey69], [Deg92], [Wil85], [Wel86], [Bar87], and [Kra92]. The results of pure E2 semi-microscopic calculations [Ass87] are presented as well (solid line). Dashed line the is s-wave capture to the D-state of ^{4}He, dash-dotted is the d-wave capture to the S-state, and the dotted line is the d-wave capture to the D-state.

on the order of a few tens of keV. The charged-particle reaction cross section at low energies is often expressed in terms of the astrophysical S-factor:

$$\sigma_{c.m.} = \frac{S(E_{c.m.})}{E_{c.m.}} \exp(-2\pi\eta), \tag{1.1}$$

where $\eta = \frac{31.29}{2\pi} Z_1 Z_2 \sqrt{\frac{\mu}{E_{c.m.}}}$ is the Sommerfeld parameter (Z_1 and Z_2 are the charges of the projectile and the target, μ is their reduced mass in AMU, and $E_{c.m.}$ is their energy in center of mass system, in keV). In this form the known effects are factored out from the cross section. The first one, $1/E_{c.m.}$, describes the "geometrical" effects: the reaction cross section $\sigma \propto \lambda^2 \propto 1/E$, where λ is de Broglie wavelength of a particle. The second factor, $\exp(-2\pi\eta)$, characterizes the tunneling of charged particles through the Coulomb barrier. Far from resonances the S-factor at low energies can be rather well represented by a linear function, which makes the extrapolation to very low energies much more straightforward.

As can be seen from Figure 1.2, the astrophysical S-factor for the ^{2}H(d, γ)^{4}He reaction can be considered as linear with energy at low energies. The calculation, presented along with experimental data, was based on microscopic treatment of the reaction, with the tensor force strength adjusted to fit the data. However, the calculation did not include coupled channels and considered only E2 radiation. Also, the big error bars of the data make the extrapolation less precise. We will see that our measurements of the polarization observables, combined with new microscopic refined resonating group model calculations, are resulting in a more reliable extrapolation of the astrophysical S-factor to low energies.

1.3 Overview of the present work

The latest experimental data showing a significant p-wave presence in the low-energy capture, and the extensive work on calculations of few-body systems using realistic potentials, were the key motivation factors for our experiment. The previous low-energy measurements performed at TUNL [Kra92] indicated that a non-E2 contribution is present, but the amount of data did not allow for a reliable transition matrix element analysis. The TME analysis of the previous experiment included E2 s-wave and E1/M2 p-wave contributions and resulted in three equally probable solutions. The calculated angular distributions for the analyzing powers corresponding to the three solutions differed mostly at back angles where no data were available.

The present experiment was designed to address the issues that arose in the previous work. In order to improve the counting rate, heavy-water ice was chosen as the target; we were able to easily refresh the target if necessary. The target chamber could be kept at high voltage to increase the beam energy and, as a result, the counting rate . The design of the target chamber allowed positioning of the detectors close to the target and at forward and backward angles while still providing space for passive shielding.

We were able to measure angular distributions of A_y and T_{20} analyzing powers at E_d=115 keV. To cross-check our data with the previous experiment, a few data points were taken at E_d=80 keV. The transition matrix element analysis included the same three TMEs: E2 s-wave and E1/M2 p-waves. We improved the analysis at E_d=80 keV: inclusion of our new data resulted in only two fits. The analysis of the 115 keV data led to a unique solution corresponding to 55% s-wave E2, 29% p-wave E1 and 16% p-wave M2 capture strength.

Preliminary results of the latest calculations based on the refined resonating group model and using realistic NN and 3N potentials, produced transition matrix elements similar to those determined by the TME analysis of our data. The final calculations are currently underway.

In Chapter 2 we will discuss the experimental setup, polarized beam production, the detector used to collect the data, and the signal processing electronics. Chapter 3 presents the analyzing power formalism and defines the transition matrix elements. It also outlines how to extract the transition matrix elements from the angular distributions. In Chapter 4 we will show how the spectra were analyzed to obtain the capture γ-ray yields used to determine the analyzing powers. The final angular distributions will be presented here as well. The transition matrix element analysis of the data is presented in Chapter 5. We will show the analysis for the 80- and the 115-keV data and the resulting fits to the analyzing powers. Finally, a brief description of the direct capture and microscopic refined resonating group models, as well as comparison of our data with the calculations will be presented in Chapter 6.

Our final goal is to provide a reliable S-factor extrapolation and to test the models that can be used to describe the reaction at very low energies. As will be discussed in Chapter 7, our experimental evidence for substantial p-wave capture leads to a correction to the energy dependence of the S-factor at very low energies. Our results indicate that the extrapolated value is about a factor of 2 lower than the previous best calculation [Ass87]. The full calculations will provide a more definite value.

Chapter 2

Experimental Setup and Methods

The vector and tensor analyzing powers for ^{2}H$(\vec{d},\gamma)^4$He reaction were measured using tensor-polarized deuteron beam from the Atomic Beam Polarized Ion Source (ABPIS). The 80-keV deuterons were accelerated to 115 keV by biasing the target chamber connected to the Low Energy Capture beam-line via an accelerator section, and then focused onto a heavy-water ice target, which was made every 4 to 6 hours inside the chamber. The capture γ-rays were observed by shielded 10" $\times$ 10" NaI(Tl) detectors and the angular distributions of the measured asymmetries for various beam polarizations were used to extract the transition matrix elements involved in the reaction. For a schematic representation of the experimental setup see Figure 2.1.

2.1 Polarized Beam

The analyzing powers arise as a result of dependence of the reaction cross section on the spin of the projectile. To measure the polarization observables we need to

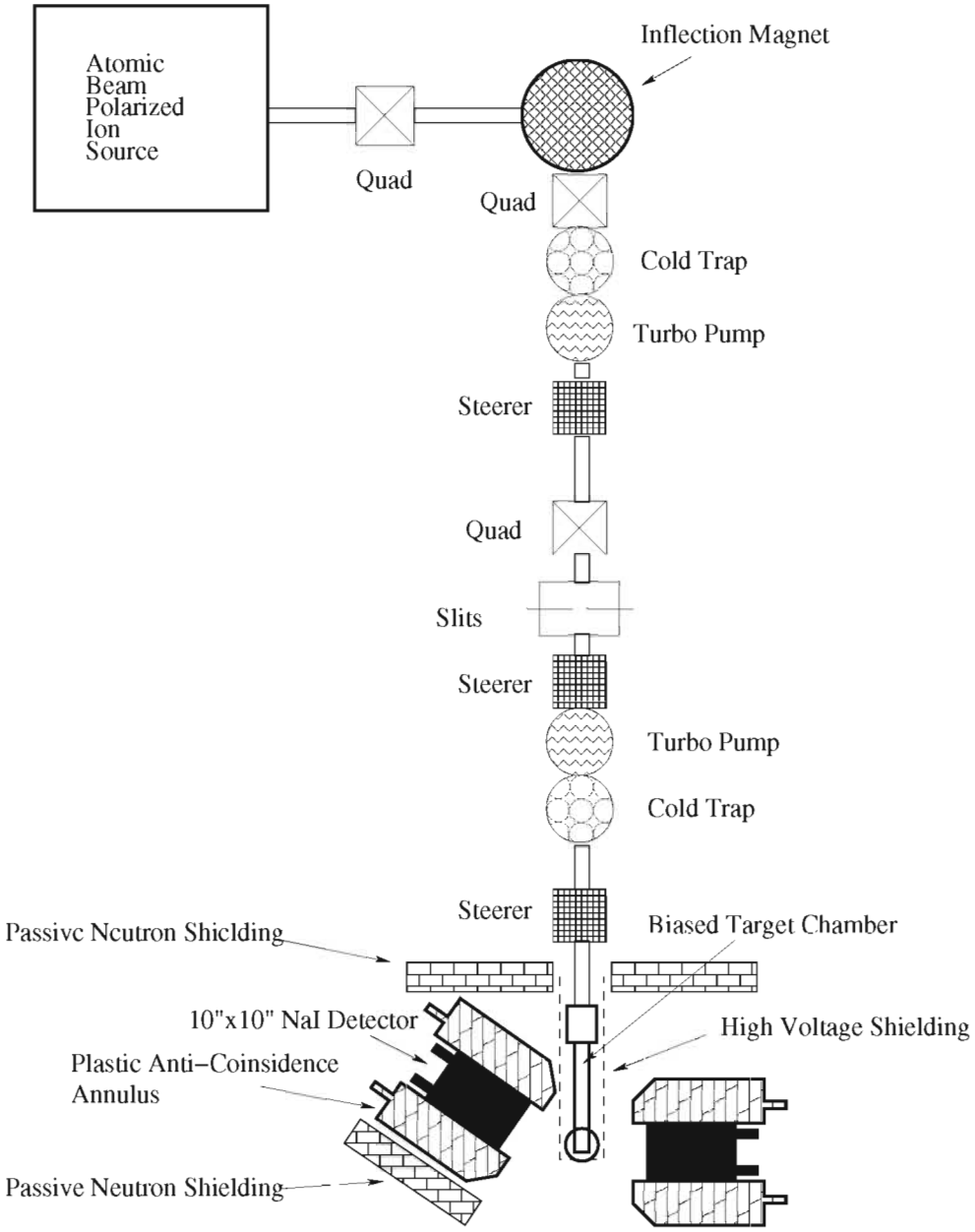

Figure 2.1: Experimental setup. Tensor-polarized deuterons are accelerated down the LECAP beam-line onto a frozen heavy-water target. The target chamber is biased to negative 35 kV and isolated from the detectors with plastic. The NaI(Tl) detectors are placed inside anti-coincidence shields. Passive shielding is set up to reduce the neutron flux into the detectors.

produce beams of known polarization, and we must be able to control both the spin state population and the spin quantization axis direction. In the following section we will discuss the appropriate terminology, the production of polarized beams and the methods of polarization measurements.

2.1.1 Beam Polarization

The beam polarization can be described via the average values of the spin operator. We will focus on the spin-one particle case, although a similar method can be applied to any spin value. The parameters used to describe the beam polarization are called tensor moments and they can be written as spherical (t_{kq}) or Cartesian (p_i and p_{ij}) tensors. We will follow the Madison Convention [Bar71] in choosing the signs and the coordinate axes. The tensor moments are related to the average values of the spin-one operator as follows:

$$
\begin{aligned}
&t_{00} = 1 \\
&t_{10} = \sqrt{\frac{3}{2}} \langle S_z \rangle \quad t_{1\pm1} = \mp \frac{\sqrt{3}}{2} \langle S_x \pm i S_y \rangle \\
&t_{20} = \frac{1}{\sqrt{2}} \left\langle 3{S_z}^2 - 2 \right\rangle \\
&t_{2\pm1} = \mp \frac{\sqrt{3}}{2} \langle (S_x \pm i S_y) S_z + S_z (S_x \pm i S_y) \rangle \\
&t_{2\pm2} = \frac{\sqrt{3}}{2} \left\langle (S_x \pm i S_y)^2 \right\rangle \\
&p_i = \langle S_i \rangle \quad i = x, y, z \\
&p_{ij} = \langle S_{ij} \rangle = \frac{3}{2} \langle S_i S_j + S_j S_i \rangle - 2\delta_{ij}
\end{aligned}
\tag{2.1}
$$

where the brackets represent the expectation value averaged over all the particles in the beam. The spin-one operator $\boldsymbol{S}$ is given by

$$S_x = \frac{1}{\sqrt{2}}\begin{pmatrix} 0 & 1 & 0 \\ 1 & 0 & 1 \\ 0 & 1 & 0 \end{pmatrix} \quad S_y = \frac{1}{\sqrt{2}}\begin{pmatrix} 0 & -i & 0 \\ i & 0 & -i \\ 0 & i & 0 \end{pmatrix} \quad S_z = \begin{pmatrix} 1 & 0 & 0 \\ 0 & 0 & 0 \\ 0 & 0 & -1 \end{pmatrix} \tag{2.2}$$

The spherical and Cartesian representations are related as follows:

$$\begin{aligned} t_{10} &= \sqrt{\frac{3}{2}}p_z & t_{1\pm1} &= \mp\frac{\sqrt{3}}{2}(p_x \pm \imath p_y) \\ t_{20} &= \frac{p_{zz}}{\sqrt{2}} & t_{2\pm1} &= \mp\frac{1}{\sqrt{3}}(p_{xz} \pm \imath p_{yz}) \\ t_{2\pm2} &= \frac{1}{2\sqrt{3}}(p_{xx} - p_{yy} \pm 2\imath p_{xy}) \end{aligned} \tag{2.3}$$

As an illustration let us consider a beam produced in a polarized ion source. In such sources of polarized particles the quantization axis for the nuclear spin, defined by the direction of the magnetic field, is typically along the beam momentum. Let us designate the quantization axis direction as $\hat{\zeta}$. The nuclear spin precesses around the magnetic field direction, and only projections on the symmetry axis have defined and non-vanishing time averaged values. For spin-one particles possible projection values are +1, 0 and -1. If the number of particles with $m_I = +1$, $m_I = 0$, and $m_I = -1$ are N_+, N_0, and N_-, then we define

$$p_\zeta = N_+ - N_- \tag{2.4}$$

and

$$p_{\zeta\zeta} = 1 - 3N_0 \tag{2.5}$$

with the rest of the p_i and p_{ij} (i.e. $i, j \neq \zeta$) being zero.

The coordinate system used to describe the analyzing tensors is shown in Figure 2.2. This is a right-handed system where the direction of the Z-axis is parallel to the

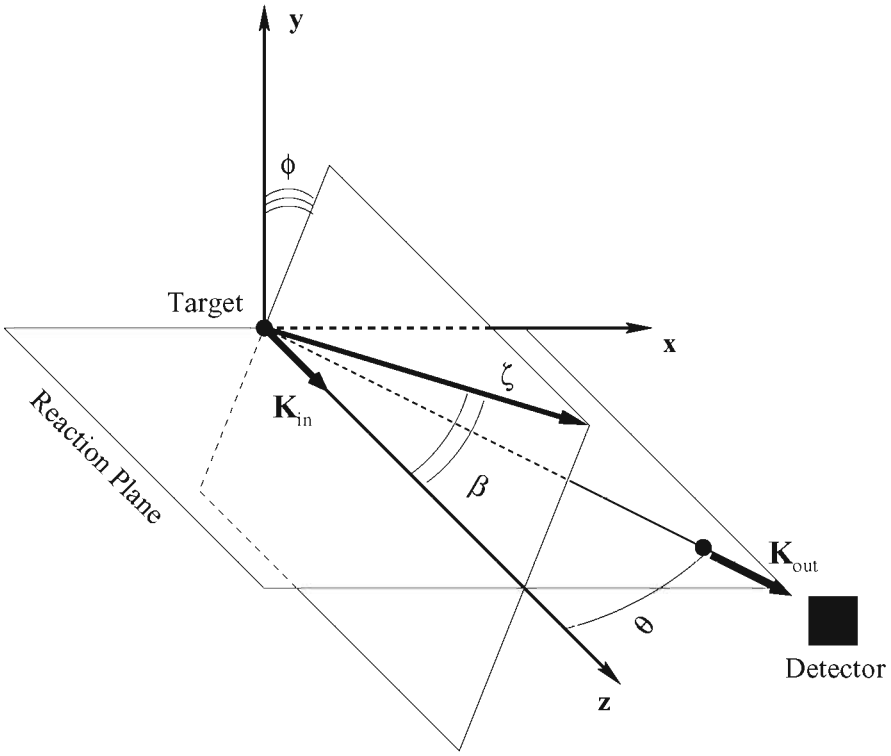

Figure 2.2: Coordinate system used to describe analyzing powers according to Madison Convention [Bar71]

momentum of the incoming particles, $\vec{k}_{in}$. The Y-axis is along $\vec{k}_{in} \times \vec{k}_{out}$, where $\vec{k}_{out}$ is the direction of the outgoing γ-ray (the angle between $\vec{k}_{in}$ and $\vec{k}_{out}$, θ, defines the position of our detector). The X-axis forms a right-handed system with $\hat{y}$ and $\hat{z}$. The spin-symmetry axis of the beam can be rotated as it leaves the polarized ion source, accommodating a particular experiment goals. The direction of the quantization axis $\hat{\zeta}$ in the Madison system is defined by two angles, β, and ϕ. The angle between $\hat{z}$ and $\hat{\zeta}$ is given by β, and ϕ is the angle between $\hat{y}$ and the projection of $\hat{\zeta}$ onto $\hat{x}$-$\hat{y}$ plane.

The analyzing powers are manifestation the of dependence of the reaction cross section on projectile spin, choosing specific polarization states (p_ζ and $p_{\zeta\zeta}$) and the quantization axis direction (angles β and ϕ) one can measure specific tensor and

vector analyzing powers. In Chapter 3 we will give the expressions relating the differential cross section to the analyzing powers and the beam polarization tensors. The production of polarized beams, and the transitions used for A_y and T_{20} measurements will be discussed in the next section.

2.1.2 Polarized Ion Source

At TUNL the polarized proton and deuteron ion beams are made by the Atomic Beam Polarized Ion Source (ABPIS),[Cle90]. The source works by producing atomic beam, polarizing the nuclear spins, ionizing the atomic beam, followed by the extraction and spin precession of the polarized ions (see Figure 2.3).

The first stage of beam production is dissociation of hydrogen or deuterium molecules. This happens in the dissociator by utilizing a gas discharge with the radio-frequency energy supplied by a TWTA (traveling wave tube amplifier). The atomic gas then diffuses into the high vacuum magnetic field region through a cold nozzle. The temperature of the nozzle is held at 30–35 K and the beam is diluted with high purity nitrogen to reduce the recombination rate.

The nuclear spin polarization region consists of two sextupole magnets and three radio-frequency transition units. The electron and the nucleus spins are coupled, resulting in hyperfine structure of the atomic levels. With no external fields the angular momentum of the nucleus, $\boldsymbol{I}$, is coupled to the electron angular momentum, $\boldsymbol{J}$, to form the total angular momentum vector $\boldsymbol{F}$, $\boldsymbol{F} = \boldsymbol{I} + \boldsymbol{J}$. Let us consider a deuterium atom in a $1s$ state. The two zero-field levels correspond to $F = 3/2$ and $F = 1/2$, with the energy gap of 1.354×10^{-6} eV (327.4 MHz) (for hydrogen it is 1420.4 MHz, the 21 cm line). In a weak magnetic field the electron and the deuteron spins

Figure 2.3: Schematic drawing of the atomic beam polarized-ion source. The hydrogen or deuterium gas is supplied into the dissociator on the left side of the figure. The gas atoms pass through the series of magnetic field and rf-transition regions, are ionized in the ECR cavity, and exit the source through the Wien filter.

are still coupled and the atomic levels are split by m_j and m_I values, according to the Breit-Rabi formula, [Bre31]. The six hyperfine levels of the $1s$ deuterium atom shown in the Figure 2.4 are labeled by the numbers in circles. The sextupole magnets focus the atoms with $m_j = 1/2$, while the atoms with $m_j = -1/2$ are removed from the beam. Referring to the Figure 2.4, only states 1, 2 and 3 pass through the sextupoles. To actually create nuclear polarization we need to produce a difference in population of the m_I levels. For a specific external magnetic field, the radio-frequency magnetic field tuned to the energy difference of the hyperfine structure states induces transitions between the states. This method is called the adiabatic-fast passage method, [Phi87]. For example, after the sextupoles we have beam with equal population of the states 1, 2 and 3. By providing a radio-frequency magnetic field with the right parameters we can induce $3 \leftrightarrow 6$ transition and depopulate the state 3 of $m_I = -1$ and populate the state 6 with $m_I = +1$, thus creating non-zero p_ζ value: a vector-polarized beam.

Typically, the analyzing power measurements require the nuclei to switch between two or more polarization states . The radio-frequency units are turned on and off to provide the rapid polarization switching. For example, for measurement of vector analyzing power A_y we needed two spin states of vector polarized deuterons, one state with p_ζ= -2/3, $p_{\zeta\zeta}$= 0 and another with p_ζ= +2/3, $p_{\zeta\zeta}$= 0. This was achieved using only the strong field transition unit for the first state, providing $1 \leftrightarrow 4$ transitions; only the second medium field unit was used for the second spin state, providing $3 \leftrightarrow 6$ transitions. For the tensor analyzing power T_{20} measurements we needed tensor polarized beam, with one state of $p_{\zeta\zeta}$= -1, p_ζ= +1/3 and another state with $p_{\zeta\zeta}$= +1, p_ζ= -1/3. The first state used the second medium field unit, transitions $2 \leftrightarrow 4$, the second state used the strong field unit, transitions $3 \leftrightarrow 5$.

The RF units are switched with a rate of 10 Hz to produce the beam of alternating

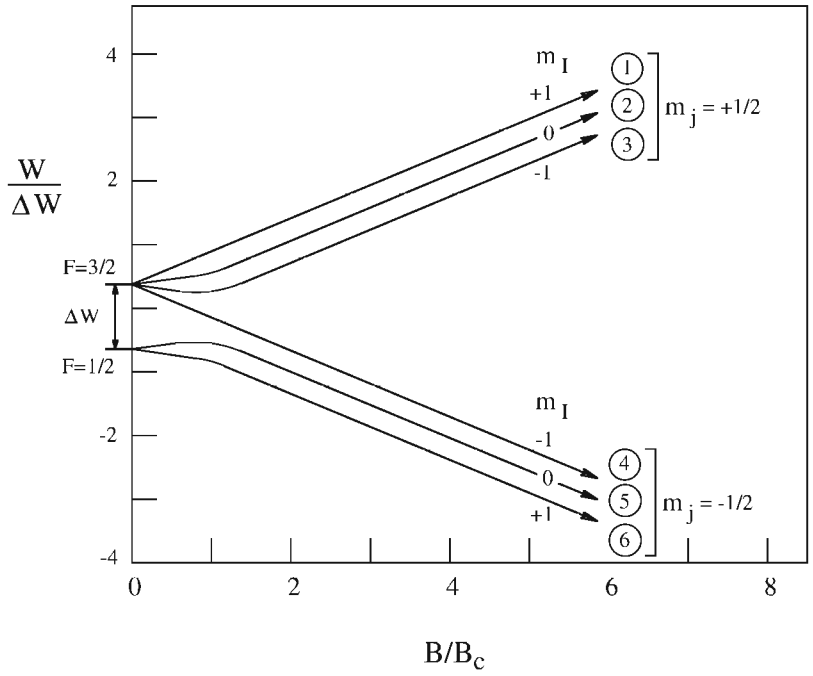

Figure 2.4: The Breit-Rabi diagram for deuterons. The sextupole magnets filter out the atoms with $mj = -1/2$ (states 4, 5, and 6). The RF transition units produce population differences of the states 1, 2, and 3, thus creating nuclear polarization of the deuteron beam .

polarization, while keeping all the other beam parameters the same. To reduce the first and second order asymmetries between + and − states, the units are switched in sequence of $+ - + + - + --$. Every time the unit is switched, a spin-veto bit is raised to disable spin sorting for 7 ms. The spin flip is driven by a clock module, and the feedback signals from the polarized source are used to set the spin state bit for the hit register. Also, every spin state switch and spin-veto bits are counted by scalar module to check the apparatus' spin state asymmetry.

After the nuclei are polarized the atoms enter the ECR (electron-cyclotron-resonance) ionizer, where the atoms are ionized by collisions with fast electrons.

The polarized positive ions pass through the cesium oven region (which can be used to produce negative beam and to measure the beam polarization with the Spin-Filter Polarimeter, see Section 2.1.3), are accelerated to 3/8 of the frame voltage and enter the Wien-filter spin precessor.

The magnetic field that produces the nuclear polarization is axial, so the spins of the particles are precessing along their momenta. Depending on experimental setup, the beam quantization axis might need to be rotated (even if we need $\hat{\zeta}$ to be along the beam momentum in the experimental area we still have to rotate the spin quantization axis in the source to compensate for the spin precession in the inflection magnets). The polarization axis rotation is performed in Wien filter, which is a region of crossed magnetic and electric fields, perpendicular to the beam momentum. The crossed fields plane can be rotated, and the field values can be adjusted to allow the beam to enter the inflection magnet and to have the polarization axis in the desired direction in the experimental area.

2.1.3 Polarimetry

There are several ways to tune and monitor the beam polarization. While use of a reaction with well known analyzing powers can be practical for monitoring the beam polarization by conducting the polarimeter measurements several times during a run, a faster procedure is preferable for the spin transitions tuning. The frequencies of the RF transition units are fixed, and the correct transitions are selected by fine-tuning the magnitude of the axial magnetic field. To monitor the effects of the tuning on the spin-state populations, the Spin Filter Polarimeter (SFP) is used.

The polarized positive ions emerging from the ECR region enter in the cesium over chamber, which is filled with Cs vapor. By charge exchange, two electrons can be added to the positive ions, resulting in negatively charged hydrogen or deuterium polarized ions. The charge exchange is only 10% efficient, which is the reason why it is preferable to utilize positive beams. The collisions of the positive ions with Cs atoms also result in production of neutral atoms. With efficiency of about 30% the atoms emerge in $2s$ meta-stable state. As the atoms de-excite, the emitted light can be detected by a photo-multiplier tube. The electromagnetic field in the SFP cavity are set up in such a way to allow only atoms of certain nuclear spin m_I pass through. The magnitude of the magnetic fields is slowly changed over a range of values to let deuterons with $m_i = +1$, -1, and 0 pass into the region of no field and de-excite. The current on the PMT is proportional to the number of nuclei of a certain m_I. By scanning over the values of the magnetic field we obtain three peaks, corresponding to the number of nuclei of different m_I: N_+, N_0, and N_- (only two peaks in case of protons). The asymmetry of the peak areas represents the spin-state population

differences, the beam polarization. The vector polarization p_ζ can be found as

$$p_\zeta = \frac{N_+ - N_-}{N_+ + N_-},$$

and the tensor polarization $p_{\zeta\zeta}$ as

$$p_{\zeta\zeta} = \frac{1 - 3N_0}{N_+ + N_0 + N_-}.$$

To use the SFP the cesium oven needs to be heated up, which takes about 20 minutes. The measurements itself requires 15 to 20 minutes, and then the oven cools down for about the same amount of time. So the whole procedure might use only one hour of the valuable running time. The spin filer polarimeter measurements were performed 2–3 times during a run, and we were relying on them to tune the transition units to maximize the beam polarization. However, the values obtained with SFP were know to differ from the ones measured by several nuclear polarimeters by 5–10%, and the numbers provided by SFP during one run had 5–10% uncertainty. This is the reason why we assumed 7% systematic error in our beam polarization values, and why we tried to double check the numbers by measurements of well known analyzing powers of $^2\mathrm{H}(\mathrm{d},\mathrm{p})^3\mathrm{H}$ reaction.

The LECAP line has a nuclear polarimeter installed, which is located just downstream from the slits. The polarimeter consists from a deuterated titanium target and two identical solid-state silicon detectors, positioned symmetrically at 110° with respect to the target. During normal running the polarimeter assembly is raised above the beam. To perform the polarization measurements the polarimeter is lowered into the middle of the beam-line, the detectors are biased to +50 Volts, and sometimes slits need to be adjusted, or the beam current has to be lowered to reduce the counting rate of the silicon detectors. For the A_y measurements setup, when the beam is vector polarized, and the quantization axis is along the $\hat{y}$-axis, the beam polarization p_ζ and

$p_{\zeta\zeta}$ can be derived from the observed asymmetries in left and right detectors. In case of T_{20} measurements, when the spin-symmetry axis is along the $\hat{z}$-axis, we have to have two spin states to observe asymmetry in one detector. The relevant formalism is discussed in Chapter 3. To illustrate the extraction of the polarization values, let us consider the case of A_y measurements with purely vector-polarized beam. To write out the expressions for beam polarization we use the relation between the cross section of a polarized-beam reaction and the analyzing powers given by Equation 3.9. For A_y measurements the beam spin-symmetry axis is setup vertically. For the left detector $\beta = 90°$, and $\phi = 0°$, the angles referring to the Madison Convention system. For the right detector $\beta = 90°$, but $\phi = 180°$. The ratio of polarized-beam to unpolarized-beam yield would be

$$\frac{Y_{lP}(\theta)}{Y_{l0}(\theta)} = \left(1 + \frac{3}{2}p_{\zeta}A_y(\theta) + \frac{1}{4}p_{\zeta\zeta}A_{yy}(\theta)\right) \tag{2.6}$$

for the left detector, and

$$\frac{Y_{rP}(\theta)}{Y_{r0}(\theta)} = \left(1 - \frac{3}{2}p_{\zeta}A_y(\theta) + \frac{1}{4}p_{\zeta\zeta}A_{yy}(\theta)\right) \tag{2.7}$$

for the right one.

The $A_y(\theta)$ and $A_{yy}(\theta)$ are known from the extensive studies of the $^2H(d,p)^3H$ reaction at low energies [Bro90], [Tag92], [Fle94]. In our case $\theta = 110°$ and the beam of 80keV is stopped in the target. We used $A_y(110°) = 0.193 \pm 0.022$ and $A_{yy}(110°) = 0.296 \pm 0.022$.

The final expressions for the beam polarization using a left-right pair of detectors are derived from Equation 2.6 and Equation 2.7

$$p_{\zeta} = \frac{1}{3A_y(\theta)}\left(\frac{Y_{lP}(\theta)}{Y_{l0}(\theta)} - \frac{Y_{lP}(\theta)}{Y_{l0}(\theta)}\right), \tag{2.8}$$

$$p_{\zeta\zeta} = \frac{1}{A_{yy}(\theta)} \left(\frac{Y_{lP}(\theta)}{Y_{l0}(\theta)} + \frac{Y_{lP}(\theta)}{Y_{l0}(\theta)} - 2 \right). \tag{2.9}$$

The errors for the tensor moment are given by

$$\Delta p_{\zeta} = \sqrt{\left(\frac{1}{3A_y(\theta)} \right)^2 D(Y(\theta))}, \tag{2.10}$$

$$\Delta p_{\zeta\zeta} = \sqrt{\left(\frac{1}{A_{yy}(\theta)} \right)^2 D(Y(\theta))}, \tag{2.11}$$

where

$$D(Y(\theta)) = \left(\frac{1}{Y_{l0}(\theta)} \right)^2 (\Delta Y_{lp}(\theta))^2 + \left(\frac{Y_{lp}(\theta)}{Y_{l0}(\theta)^2} \right)^2 (\Delta Y_{l0}(\theta))^2 + \left(\frac{1}{Y_{r0}(\theta)} \right)^2 (\Delta Y_{rp}(\theta))^2 + \left(\frac{Y_{rp}(\theta)}{Y_{r0}(\theta)^2} \right)^2 (\Delta Y_{rp}(\theta))^2, \tag{2.12}$$

end the errors in the yields are statistical, i.e. $\Delta Y_i(\theta) = \sqrt{Y_i(\theta)}$.

Such polarimetry measurements were performed and were in agreement with the SFP results. To obtain the correct values of p_{ζ} and $p_{\zeta\zeta}$ one needs to run both polarized and unpolarized beams, with known amount of beam on target in every case. Unfortunately, because of lack of electronics, we could not have our NaI setup and the polarimeter setup at the same time, that's why the polarimeter measurements were performed only a few times to cross check with the SFP measurements. The results of one of such measurements are presented in Table 2.1 and Table 2.2.

Spin state	p_{ζ}	$p_{\zeta\zeta}$
MF2	-0.599	-0.011
SF2	+0.439	-0.077

Table 2.1: SFP measurements during December 2000 A_y run.

Spin state	Y_l	Y_{l0}	Y_r	Y_{r0}	p_ζ	$p_{\zeta\zeta}$
MF2	28703	36734	48259	40146	-0.73±0.02	-0.06±0.02
SF2	41983	36734	34883	40146	+0.47±0.02	-0.04±0.02

Table 2.2: Nuclear polarimeter measurements during December 2000 A_y run. The yields were obtained during three measurements with unpolarized and two polarized states. The total charge on the target in each spin state was equal.

One more way to check the beam polarization during a run was to utilize the silicon detector mounted on the target chamber. Because the detector is in the vertical plane (see Figure 2.6), it could be used only during T_{20} measurements, when there is no azimuthal dependence in yields. During such runs we were able to observe asymmetry in the spin-sorted silicon detector spectra, and using known $T_{20}(150°)$ for E_d=115keV we were able to check p_ζ and $p_{\zeta\zeta}$. Again, the measured values were close to the ones provided by the Spin Filter Polarimeter.

2.2 Beam Transport and Target

One of the major difficulties in studying $^2H(\vec{d},\gamma)^4He$ is the low counting rate of the capture γ-rays (the total cross section of the reaction is on the order of nanobarns). Previous measurements by Kramer *et al* [Kra92] at E_d= 80 keV, the energy of the beam directly out of the ABPIS, involved the use of a deuterated titanium target, close geometry, high beam current (about 30 μA) and observed approximately 10 counts per hour. We have made a number of changes in an attempt to increase the counting rate. One of these changes involved designing a new target chamber capable of being biased up to negative 60 kV. This was a way to raise the beam energy and thus to increase the cross section of the reaction, while not changing mechanism of the reaction (most of the data was actually taken with 35 kV on the chamber,

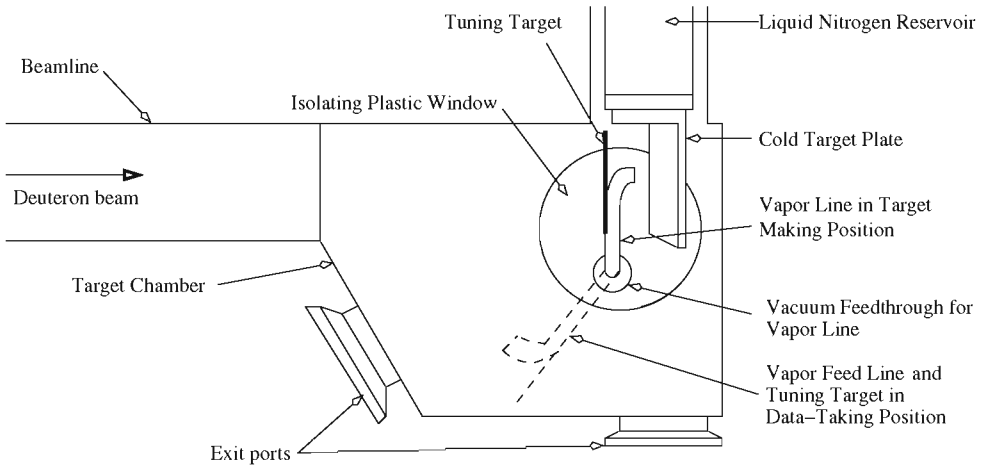

Figure 2.5: The side view of the target chamber. The vapor line can be rotated to face the cold target plate for ice-target production. In this position the tuning target can be used to measure the beam current. During data-taking the tuning target and the vapor line are rotated out of the beam.

corresponding to a beam energy of E_d= 115 keV).

The target chamber was connected to the rest of the beam-line via an acceleration section. The downstream part of the acceleration section was connected to a Glassman high voltage power supply. To electrically isolate the chamber from the ground, the chamber was enclosed in a plastic shield (1/4" thick Plexiglas) which also served as a support for the chamber. The chamber itself consisted of 1 meter long pipe connected to a narrow target box. The long piece was necessary to allow positioning the detectors at back angles without being too close to the accelerator section. On top of the box there was a liquid nitrogen dewar with a cold finger connected to the aluminum target paddle. The box also had a pump-out port on the bottom and a port for the silicon detector assembly. On one side the box had a 3 " window covered with a Plexiglas cap, which allowed for visual inspection of the target. The cap had a feed-through for a pipe that carried the heavy water vapors from the water bottle

onto the cold target paddle. The water pipe could be rotated in the cap from the target making position to the normal running position. While making a target, the pipe was pointed to the cold paddle and the water vapor would freeze on the paddle producing the ice target. The water pipe also held the tuning target: a thin metal piece of approximately the same size as the target. It was used to read out the beam current that would hit the target. Normally, the beam current was checked every time a new target was made. During normal running the water pipe and the tuning target were rotated out of the way of the beam and of the protons going into the silicon detector. Because the whole chamber was biased, nothing at this point was connected to the tuning target. Since we were unable to read the beam current directly off of the biased target chamber and since the target thickness varied with time, some means of beam and target quality monitoring were necessary. For this purpose we utilized the $^{2}\mathrm{H}(\mathrm{d},\mathrm{p})^{3}\mathrm{H}$ reaction. The protons produced by this reaction were counted by a solid-state detector placed at the end of a plastic tube, connected to one of the ports of the target box, see Figure 2.6. The silicon detector was in the vertical plane at 150°with respect to the beam direction, and subtended a solid angle of $\sim$ 150 μsr. The detector assembly was separated from the chamber with a 1/20 mil (1.27 μm) thick nickel foil. The foil stopped the tritons but the protons of 2.7 MeV passed through it. The foil was grounded to stop the scattered from the target and the chamber electrons in order to prevent noise and pile-up distortion of the monitor spectra. The silicon detector was biased to +50 V and produced very clean spectra, see Figure 2.7. A typical count rate in the monitor detector was on the order of tens of counts per second, so we could immediately notice if the target was starting to deteriorate. Figure 2.8 shows the changes in the monitor detector counting rate. As the rate starts dropping, a new target is made. A typical period between

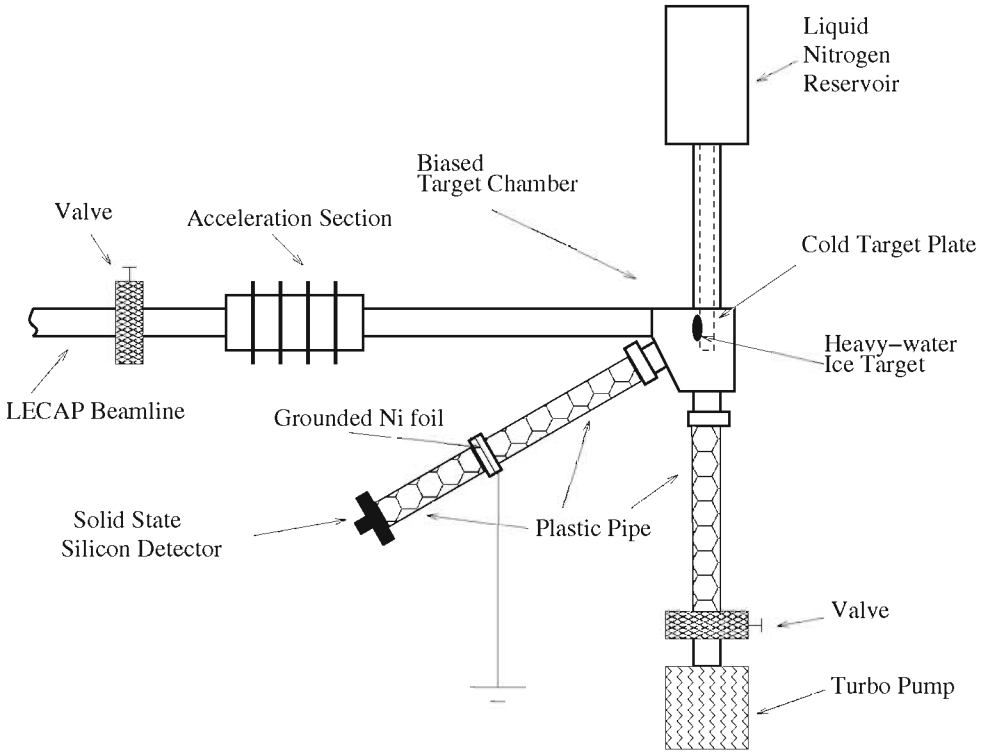

Figure 2.6: Side view of the biased target chamber setup. The chamber was supported by the liquid nitrogen dewar, which bottom was resting on the plastic high voltage shielding. The valves were closed during evaporation of heavy water onto the cold target plate. The use of non-conductive plastic tubes allowed us to place the pump and the silicon detector at ground potential.

making of new targets was 4–6 hours. Also, in particular cases (T_{20} measurements) the monitor reaction was used to cross check the values of the beam polarization by measurement of T_{20} for the $^2H(d,p)^3H$ reaction at 150°, and comparison with the results of previous measurements (numerous studies of the reaction at low energies, [Bro90], [Tag92], [Fle94]).

The compact geometry of the chamber make it possible to position the detectors rather close (10") to the target, providing a solid angle of about 3 sr.

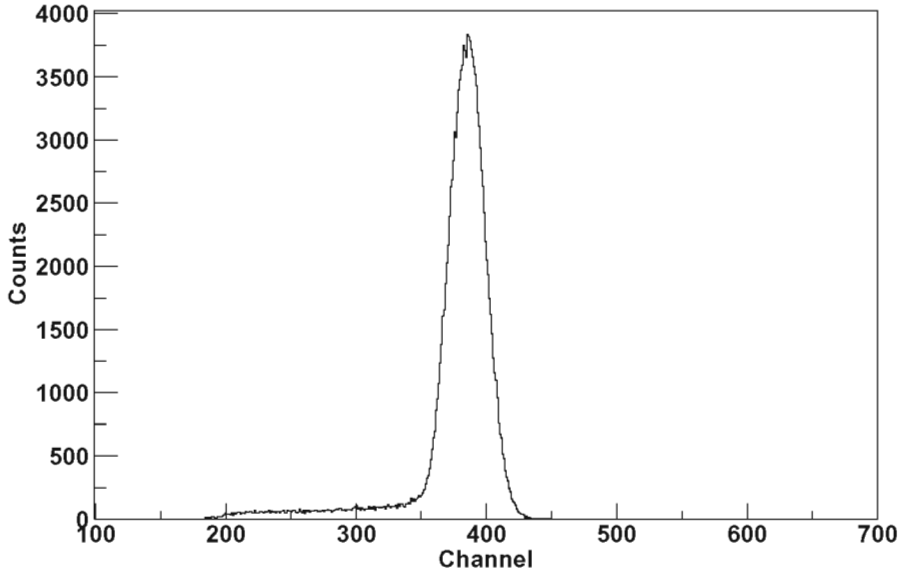

Figure 2.7: A typical spectrum produced by the silicon detector. The threshold is set below the 2.7 MeV proton peak. The presented spectrum is for one-hour run and corresponds to proton counting rate of 40 Hz.

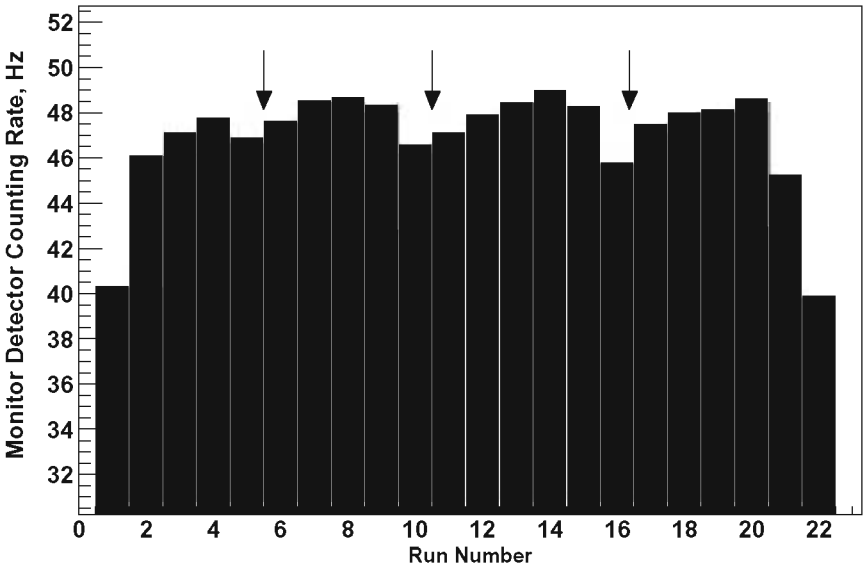

Figure 2.8: An example of using the silicon detector for target quality monitoring. When the monitor detector count rate started to drop, a new ice target was made (shown by the arrows).

2.3 NaI(Tl) Detectors

2.3.1 Physics of γ-ray-detection

The reaction produces γ-rays of rather high energy (Q = 23.8 MeV). NaI(Tl) crystals are some of the most efficient scintillators at this energy region. They also have acceptable energy resolution to adequate separate the capture peak from the slowly varying background.

To understand what defines the efficiency and the energy resolution of a detector, and the features observed in a spectrum, it is critical to know what is the mechanism of converting the γ-rays into the light detected by the photo-multiplier tubes (PMTs) connected to the scintillator. There are three major processes by which γ-rays interact with matter: the photo-electric effect, Compton scattering and the pair-production. At lower energies (below 1MeV) the photo-electric effect dominates. In this process all of the γ-ray energy is absorbed by a bound electron of an atom. This results in the emission of X-rays or Auger electrons. The low-energy X-rays are absorbed by secondary photo-electric events, and the electrons deposit their energy by collisions (excitation and ionization of atoms), and radiation (bremsstrahlung). The radiative energy loss for electrons in sodium iodide overcomes the collision loss only at energies above 1 MeV. In the Compton scattering the incoming γ-ray transfers part of its energy to an electron. The energy of the electron vary from zero up to a maximum value. In case if all of the Compton scattered photons and electrons are converted into visible light we observe the full-energy peak, corresponding to the energy of the original γ-ray. Meanwhile, some of them can escape out of the detector and it leads to the low energy Compton scattering structure in the spectra. Finally, at energies higher than 1022 keV electron-positron pair production becomes possible. The produced

electrons and positrons lose their energy through collision and radiation, and when the positron is slowed down to thermal energies it annihilates with an electron, emitting two 511 keV γ-rays 180° with respect to each other in the center of mass frame. One of those γ-rays can escape the crystal, thus 511 keV of the original γ-ray energy is lost. These events lead to the appearance of escape peaks: the first escape peak, 511 keV lower than the full energy peak, if one of the annihilation γ-rays escaped; and the second escape peak, 1022 keV lower than the full energy peak, if both of the annihilation gammas escape the crystal. We were able to observe the first escape peaks (and actually use them for calibration) in the Am-Be source spectra (an example is given on Figure 2.9). The source produces 4.4 MeV γ-rays, and the first escape peak for this energy is clearly resolved, see Figure 2.9. At high energies though, like in the case of $^2\mathrm{H}(\vec{d},\gamma)^4\mathrm{He}$ capture γ-rays (23.8 MeV) the full energy peak and the escape peaks are not resolved as separate peaks. For this reason, and to have higher statistics, the γ-rays that did not deposit their full energy (first escape events) were not rejected by the anti-coincidence shield. This was accomplished by setting the discriminator level on the shield signals at a level above that needed to detect 511 keV γ-rays.

The cross section of γ-ray interaction with a NaI crystal is shown in Figure 2.10. At energies above 10 MeV the pair-production is the dominating process. The cross section of pair-production depends on Z^2, and because the average atomic number Z of NaI is rather high, NaI detectors are very widely used for high energy spectroscopy. At lower energies the efficiency of NaI detectors is even higher, but the energy resolution is not as good as that for high purity Ge detectors (although NaI detectors still find lots of use for low energy experiments, being cheaper and easier to maintain than HPGe). At higher energies (above $\sim$20 MeV) the efficiency of HPGe is several orders

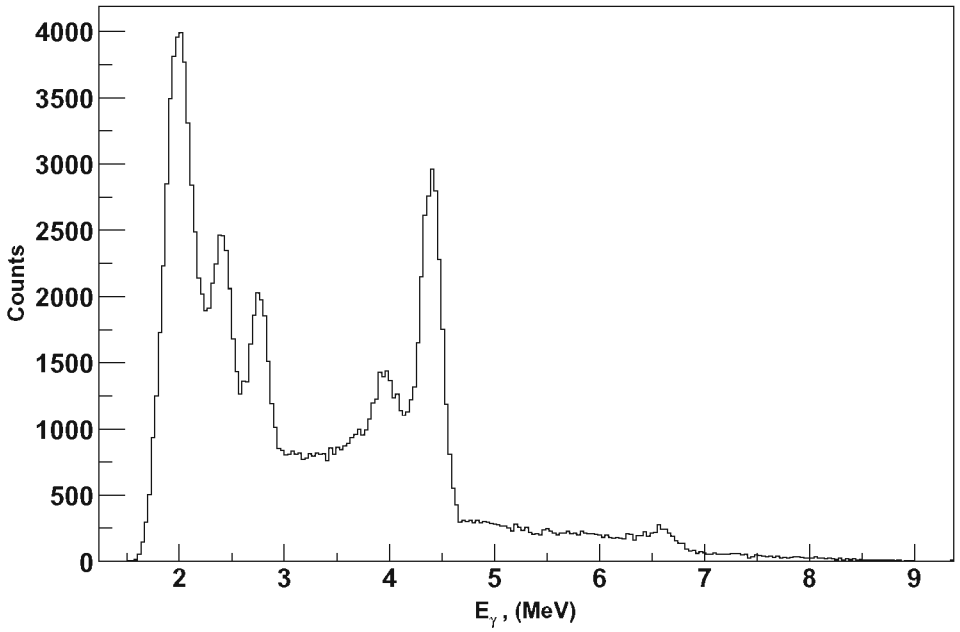

Figure 2.9: Calibration spectrum for a NaI(Tl) detector with an Am-Be source. The major source line is 4.4 MeV, result of de-excitation of ^{12}C produced in α-capture on ^{9}Be. The first escape peak at 3.9 MeV is also visible. The 6.8 MeV peak is due to the radiative capture of neutrons on iodine of the crystal. The two visible natural background peaks are the 2.2 MeV line (radiative capture of thermal neuterons on protons) and the 2.6 MeV line of ^{226}Th.

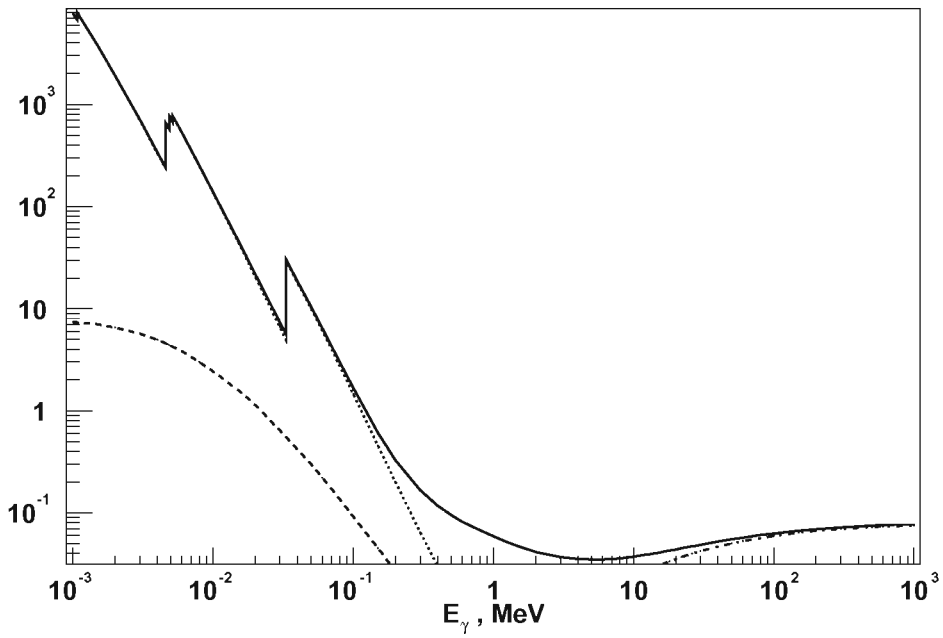

Figure 2.10: γ-ray interaction with NaI crystal. At low energies photo-electric effect (dotted line) and scattering (dashed line) dominate, while at energies above 10 MeV most of the γ-ray energy is deposited through the pair-production (dash-dotted line) The total cross section is shown with the solid line.

of magnitude less than that of NaI. The NaI crystal is doped with thallium to create the activator states in the band gap of NaI and as a result to slightly increase the scintillation photon wavelength. This reduces self-absorption in the crystal and moves the scintillating light into the region of more efficient photon-electron conversion in the photo-multiplier tubes.

2.3.2 Detector Design

The NaI(Tl) crystal is viewed by 6 PMTs. All the tubes were gain-matched by adjusting the applied high voltages to match the positions of natural background peaks and the 4.4 MeV line of an Am-Be source seen by different photo-multipliers. Later the signals are fanned in and the gain-matching provides better timing quality of the summed signals. For pile-up rejection it is preferable to have signals with short tails. For this reason the PMT signal cables were coupled with to a delay line of about 100 ns (20 meters) with the terminating resistor adjusted to make the signals as short as possible, without overshoot, and without diminishing the resolution in the resulting spectrum.

Cosmic rays produce substantial background. To suppress this, the NaI(Tl) detectors were placed in plastic anti-coincidence shields (10 cm thick Bicron BC412 annulus). The plastic scintillator does not have good energy resolution but produces very fast signals (on the order of 10 ns). The shield scintillator was viewed by 8 PMTs which were fanned in and connected to the cosmic ray rejection circuit (see Section 2.4). A cosmic ray would deposit energy in both the shield and the central crystal. That would produce a coincidence event between the NaI(Tl) and the shield, and the event would be "vetoed"; not used for the analysis. But another possibility for such a coincidence event is a detection of a "valid" γ-ray which produced an

electron-positron pair that deposited most of its energy in the crystal, but one of the positron-annihilation γ-rays escaped the detector and deposited its energy in the shield – first escape event in the detector. As previously mentioned, to accumulate better statistics such events needed to be considered (not vetoed), and so the threshold on the shield signals were set above 0.511 MeV (about 1 MeV). More on threshold settings for the NaI(Tl) detectors and the shields is described in Section 2.4.

Another important source of background and a major reason for utilizing the pile-up rejection is neutron-induced background. Neutrons produced via the $^{2}\mathrm{H(d,n)}^{3}\mathrm{He}$ reaction thermalize in surrounding materials, enter the NaI(Tl) crystal and capture on the iodine nuclei. As the iodine nucleus de-excites it emits γ-rays of energies in the vicinity of 6.8 MeV(the Q-value for the neutron radiative capture on ^{127}I, the most abundant isotope of iodine, is 6.8 MeV). Because these γ-rays are produced inside the crystal they are absorbed with high efficiency. Because the cross section of $^{2}\mathrm{H(d,n)}^{3}\mathrm{He}$ reaction at low energies is about seven orders of magnitude higher than of $^{2}\mathrm{H}(\vec{d},\gamma)^{4}\mathrm{He}$, the overwhelming neutron capture signals can lead to such problems as pile-up and gain-shifts in the PMTs. To reduce the amount of neutrons entering the NaI crystal we added paraffin, bricks of borated polyethylene and lithium carbonated paraffin around the detector. An 0.8 mm cadmium sheet was placed around the anti-coincidence shield to convert the neutrons into γ-rays (via the neutron radiative capture), and finally, lead sheets were wrapped around th annulus to attenuate the γ-rays entering the detector. The passive shielding proved to be very useful for low-energy background suppression.

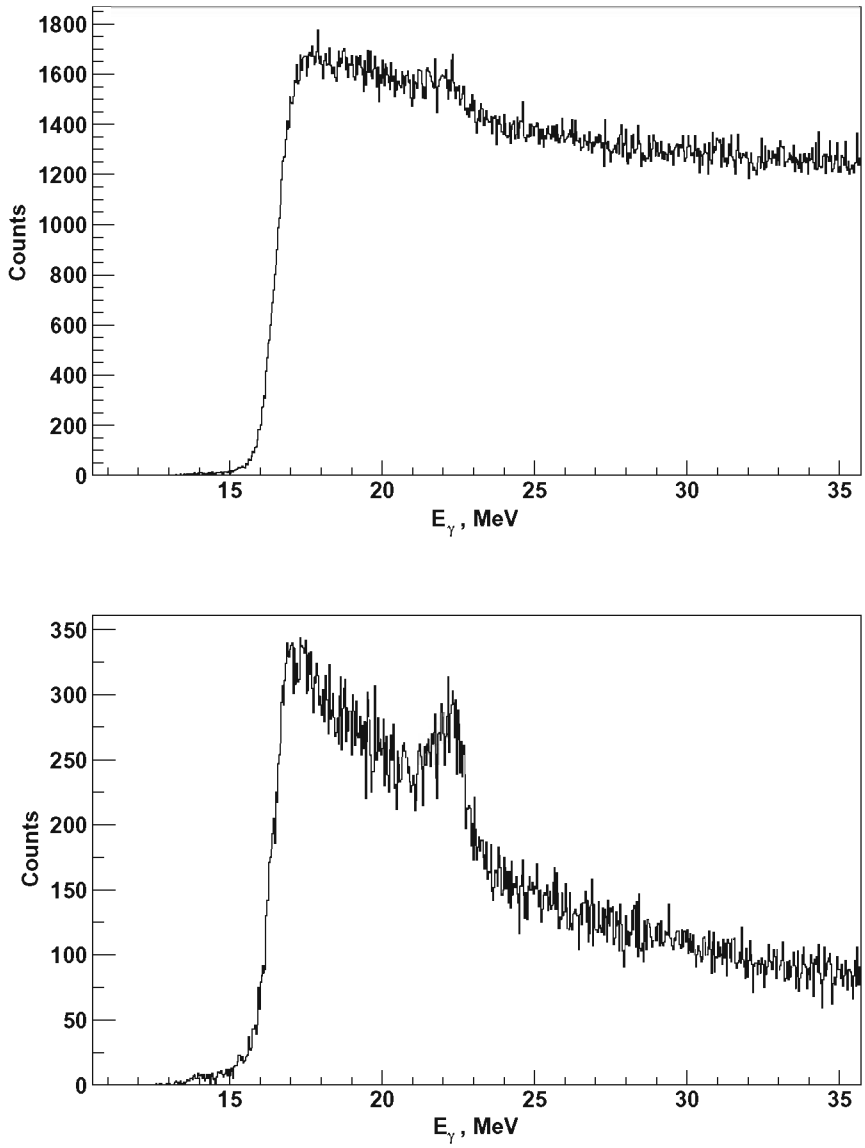

Figure 2.11: Energy spectra produced from a NaI(Tl) detector. Both are results of week-long measurement. The top one is the raw signal, everything that is seen by the detector. The bottom one is produced by vetoing cosmic-ray induced events in the raw spectrum.

2.4 Electronics

The electronics setup can be divided into three branches: the NaI(Tl) detector energy branch, the detector trigger branch and the anti-coincidence shield trigger branch (see Figure 2.12).

Because out peak of interest lies above 20 MeV there are no radioactive sources to use for calibration or delay line tuning. Therefore, signals from cosmic rays are used for setting up timing, thresholds and of course, for determining the cosmic-ray rejection rate.

The clipped energy signals are fanned in (just using "'T"-connectors) and sent to the control room via low loss cables. At this point the NaI(Tl) detector signal is split into linear and logic signals by fanning out using a LeCroy 128 Fan Out module. One copy of the signal goes through a delay line of about 300 ns before being sent to the linear input of a Tennelec TC308 linear gate. Another copy goes through set of discriminators and gate-and-delay generators to produce triggers for the energy signal and to provide pile-up rejection. First, the signal is sent through an Ortec 454 Timing Filter Amplifier (TFA). The signal is shaped into a shorter bipolar signal with rise-time of about 20 ns. The output of the TFA is sent into an EG&G TD101 leading edge "differential" discriminator. The discriminator is operated in Lower Level Threshold mode. In this mode the timing of the output logic pulse is determined by the setting of the lower level (E), while the threshold is set by the sum of the lower level and the window ($E + \Delta E$). E is set rather low, corresponding to γ-ray energy of about 1 MeV. This results in a smaller time jitter in the trigger pulses for different signal input pulses and thus enables setting of a tight coincidence gate for the purpose of cosmic-ray rejection. Settings of the TFA gain and TD101

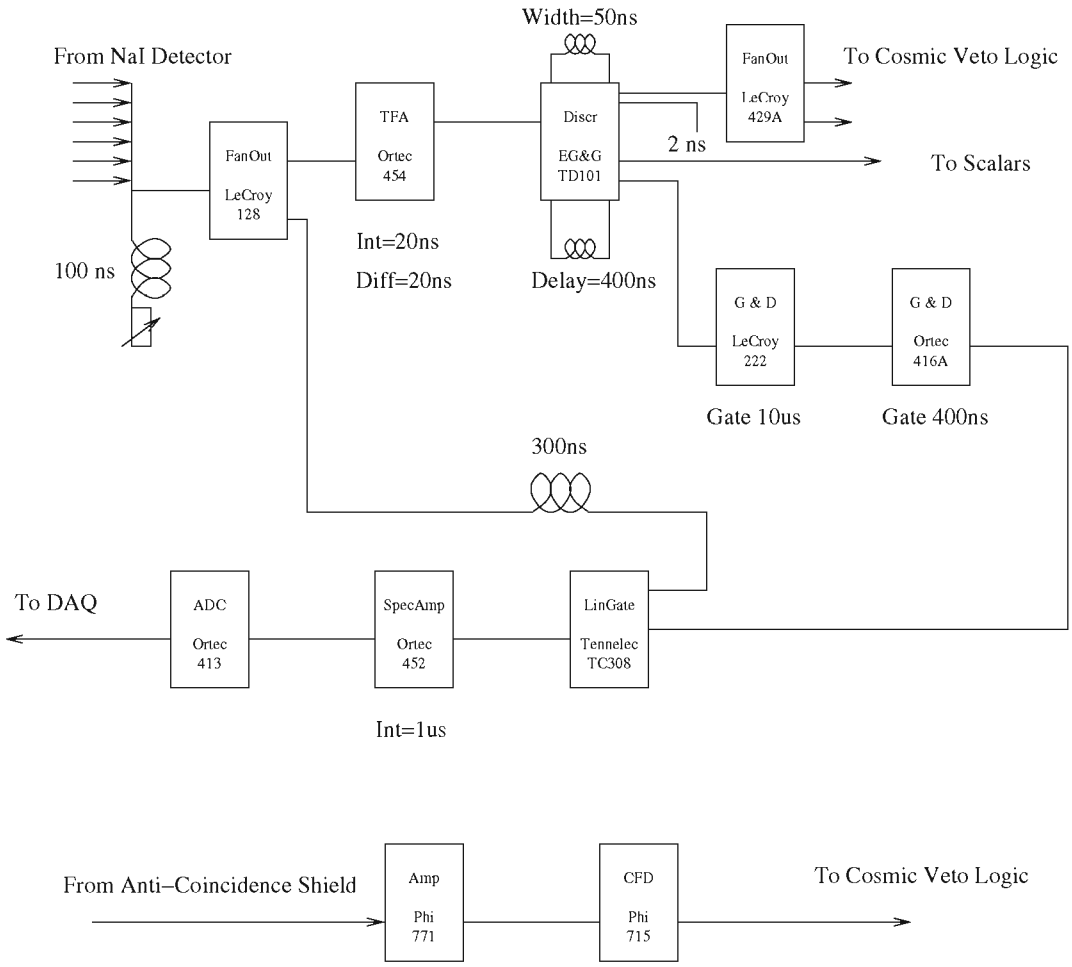

Figure 2.12: The electronics diagram for the NaI(Tl) detector. Utilization of pulse shaping with the clipping line and TFA, and fast linear gate setup, helps to reduce pile-up in spectra. A copy of the discriminator output is tested for coinsidence with the plastic shield detector. In event of considence the cosmic-ray veto bit is set to reject the event.

threshold define the total threshold for the NaI(Tl) energy pulses. It can be fine-tuned by changing ΔE, without changing the timing of the system. The shaping of the linear signal with the TFA and sending it through a fast discriminator is the core of the low-low pile-up rejection technique being employed. Any two small (below the discriminator threshold) signals separated by more than 20 ns after shaping by the TFA will be treated as separate signals and will not trigger the discriminator. This eliminates low-low pile-up on 20 ns scale. The output of the discriminator is sent to a LeCroy 222 Gate-and-Delay generator (G&D) set to have a gate width of 10μs. The long logic pulse is set to trigger another G&D generator (Ortec 416A), output of which is used as the gate for the delayed copy of the energy signal. The width and position of this logic signal is adjusted to enclose the linear signal (about 400 ns wide). After the timing of the gate and the linear signal are set, they are sent through the fast Linear Gate (Tennelec TC308), which is open only to the signals that pass the threshold and are not closer than 10 μs apart. The use of the "long gate – short gate" setup provides reduction of high-high and high-low pile-up. If the discriminator is triggered by a pulse, which is followed by another one, below or above the threshold, the second pulse will not be included in the linear gate if it comes later than 400 ns from the trigger. Thus the high-low and high-high pile-up is reduced on 400 ns scale, defined by the width of the short gate. The long gate is necessary to prevent distortion of the signal during conversion by the Analog-to-Digital Converter (ADC) Ortec 413, the final and the slowest part of the circuit. During the conversion the discriminator may trigger again on the next pulse, but it will be ignored by the ADC until the current pulse is digitized. It is important to check the quality of the linear signal and the Linear Gate pedestal. The amplitude of the PMT signals is on the order of 100 mV for 10 MeV γ-rays. If the baseline of the energy signal has substantial

low frequency noise, or the pedestal of the Linear Gate (the DC offset that is added to the linear signal while passing through the linear gate) changes randomly, the energy resolution of the system might become unacceptable, prohibiting calibration and the peak extraction from the spectra. The output of the linear gate goes through a spectroscopy amplifier (Ortec 452) to shape and amplify the NaI(Tl) detector energy signal, producing an output signal of a few volts in amplitude (0–10 V full scale) and about 1μs long. That signal is patched to the ADC.

A copy of the output of the TD101 discriminator is sent to a scalar, counting the raw number of events that were triggered. The gate that was used in the fast Linear Gate is also sent to the CAMAC crate to serve as a gate for the ADC. The Ortec413 was used in the common gate mode because the fixed event size in XSYS prohibits using the single gate mode and as well as providing for more efficient use of the ADC. Because two NaI(Tl) detectors were normally used at the same time, they were patched to different channels of the ADC and the gates for both energy signals were added and then sent to the common gate of the ADC. In addition to the energy signals, the gates, and the scalars, a number of additional signals were sent to the BiRa 2351 hit register. The hit register was read out with every event and it provided logic bits used to sort the incoming energy signals into various spectra. The signals going into the hit register included the copies of the trigger gates serving as bits to determine which detector produced the signal, and the cosmic ray rejection bits which were produced by a coincidence between the NaI(Tl) detector and the plastic shield.

The cosmic ray rejection branch incorporates an amplifier (Phillips 771), a Constant Fraction Discriminator (CFD) Phillips 715 and a logic module Ortec C04020. The first two are used to set the threshold on the shield energy signal and produce a logic signal, which is then sent to the logic module, to be tested for coincidence with

a copy of NaI(Tl) detector trigger. As was discussed in the Section 2.3 the thresholds on the shields were set to be just above 511 keV to reject the events produced by cosmic rays, γ-rays that did not deposit their full energy in the NaI(Tl) crystal, but to keep the first-escape events in which only 511 keV of the full energy of an incoming γ-ray is lost. The shield threshold was set after the NaI(Tl) branch was set up, so the trigger rate and timing of the triggers for the detector would not be disturbed while setting the rejection rate. The shield threshold was adjusted by lowering the CFD threshold or by raising the amplifier gain and measuring the coincidence rate between the shield and the NaI(Tl) crystal. As the threshold is lowered the coincidence rate would peak at about 98 – 99 % and then drop, as the noise region in the shield was being sensed. When the rejection rate was maximized, the vetoed spectra (NaI(Tl) energy spectra corresponding to coincidence between the crystal and the annulus) were checked using the Am-Be source. If the vetoed spectra did not have a peak corresponding to the first escape events of the 4.4 MeV peak, the threshold setting was taken to be acceptable.

Because the cosmic ray rejection is defined by a coincidence condition, special care had to be taken in setting up the timing between the NaI(Tl) detector and the shield triggers. The detector triggers are produced by the TD101 discriminator, they are about 10 ns wide, and their timing is stabilized by using the lower level threshold for the discriminator. The width of the shield triggers (about 60 ns) and the timing between the shield and the detector signals were set up so that the NaI(Tl) signal is always inside the shield. The timed logic signals from the detector and the shield were fed into an Ortec C04020 Logic Module to produce the cosmic ray veto bits. They were patched to the hit register to be used for sorting.

The energy spectra of the protons produced in the $^{2}\mathrm{H}(\mathrm{d},\mathrm{p})^{3}\mathrm{H}$ reaction were

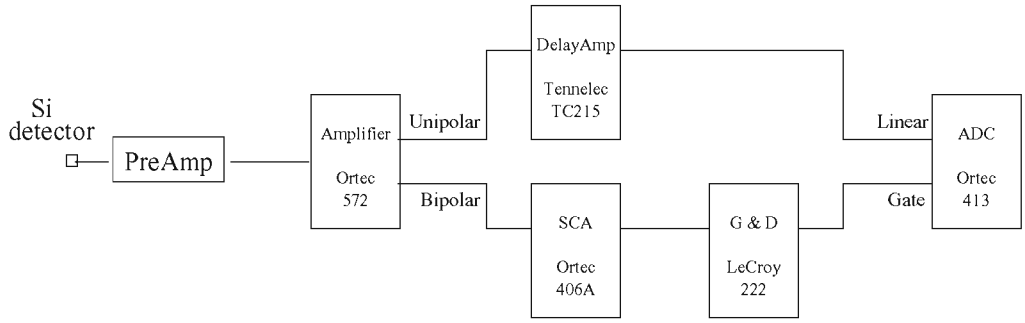

Figure 2.13: The electronics diagram for the silicon solid-state detector

digitized and sorted into histograms according to the spin state. The electronics used for the silicon solid-state detector is very standard (see Figure 2.13). The energy signal is preamplified and patched to an Ortec 572 amplifier. The unipolar output of the amplifier, after passing trough a Tennelec TC2515 delay amplifier, is sent to the ADC. The bipolar output goes through a single channel analyzer (SCA) Ortec 406A to produce the trigger signal. The timing of the trigger and the output of the delay amplifier is adjusted so that the logic signal encloses the linear signal and can be used as the gate for the ADC. Another copy of the trigger signal is sent to the scalar module to be used for the monitor detector count rate calculation.

2.5 Data Acquisition

The NaI(Tl) detector energy signals, detector trigger, cosmic-ray veto, accidental coincidence bits as well as the silicon detector energy signal and trigger bit were patched to CAMAC crate. Linear signals were digitized by an Ortec 413 peak-sensing ADC, while the bits, along with the spin-state bits from the ABPIS were read in with a BiRa 2351 Hit Register. The CAMAC crate is controlled by a Micro-programmable

Branch Driver (MBD) manufactured by the BiRa Corporation. The MBD is connected to a MicroVAX 3200 computer running the data acquisition and analysis software TUNL XSYS. This system allows the user to control which modules are being read out, what the event format is, and how the digitized data is sorted (more about it in Chapter 4, Section 4.1). The resulting histograms were used for online monitoring and stored on disk for offline analysis.

Chapter 3

Polarization Observables

Yields of the capture γ-rays at different angles and spin states are used to determine the angular distributions of the various analyzing powers. The analyzing powers can be related to the transition matrix elements (TMEs) involved in the reaction. In this chapter, we will discuss which TMEs are considered in the reaction and how they are extracted from the observed angular distributions.

3.1 Analyzing Powers As Asymmetries

Let us first consider how polarized beams can be used for measurements of analyzing powers.

The differential cross section for a reaction initiated by a beam with tensor components t_{kq} is given by

$$\sigma = \sigma_0 \sum_{k,q} \mathrm{t}_{kq} \mathrm{T}^*_{kq}, \tag{3.1}$$

where σ_0 is the cross section for unpolarized beam and the $\mathrm{T}^*_{kq} = (-1)^q \mathrm{T}_{k-q}$ are the tensor analyzing powers. The beam polarization and the analyzing powers can be written as spherical or as Cartesian tensors. The relationships between the two representations are given in Chapter 2, Section 2.1.1, Equation 2.3. Parity conservation implies that $\mathrm{T}_{10} = 0$, T_{11} is purely imaginary and T_{2q} are real. For a spin-one beam, the cross section can be written in terms of spherical tensors as

$$\sigma(\theta) = \sigma_0(\theta)\Big(1 + 2\Re(i\mathrm{t}_{11})i\mathrm{T}_{11}(\theta) + \mathrm{t}_{20}\mathrm{T}_{20}(\theta) + 2\Re(\mathrm{t}_{21})\mathrm{T}_{21}(\theta) + 2\Re(\mathrm{t}_{22})\mathrm{T}_{22}(\theta)\Big) \tag{3.2}$$

where $\Re$ represents the real part.The same can be expressed via Cartesian tensors

$$\sigma(\theta) = \sigma_0(\theta)\Big(1 + \frac{3}{2}\mathrm{p}_y\mathrm{A}_y(\theta) + \frac{1}{2}\mathrm{p}_{zz}\mathrm{A}_{zz}(\theta) + \frac{2}{3}\mathrm{p}_{xz}\mathrm{A}_{xz}(\theta) + \frac{1}{6}(\mathrm{p}_{xx} - \mathrm{p}_{yy})(\mathrm{A}_{xx}(\theta) - \mathrm{A}_{yy}(\theta))\Big) \tag{3.3}$$

The beam polarization tensors and the analyzing powers here are referred to the coordinate system of the so-called Madison Convention, discussed before in Section 2.1.1 and shown in Figure 2.2.

It is convenient to express the beam polarization in terms of the "internal" polarization moments, i.e. with respect to a system in which the third axis is the spin-symmetry axis of the beam, $\hat{\zeta}$. In this system most of the polarization moments p_κ and $\mathrm{p}_{\kappa\lambda}$ (or $\tau_{\kappa\lambda}$ as corresponding spherical tensor) vanish, leaving only p_ζ and $\mathrm{p}_{\zeta\zeta}$ (or τ_{10} and τ_{20}) with finite values. The ABPIS produces polarized beam with particular values of p_ζ and $\mathrm{p}_{\zeta\zeta}$. The spin-symmetry axis $\hat{\zeta}$ can be rotated using the Wien filter, and the final beam polarization moments of Equation 3.2 and Equation

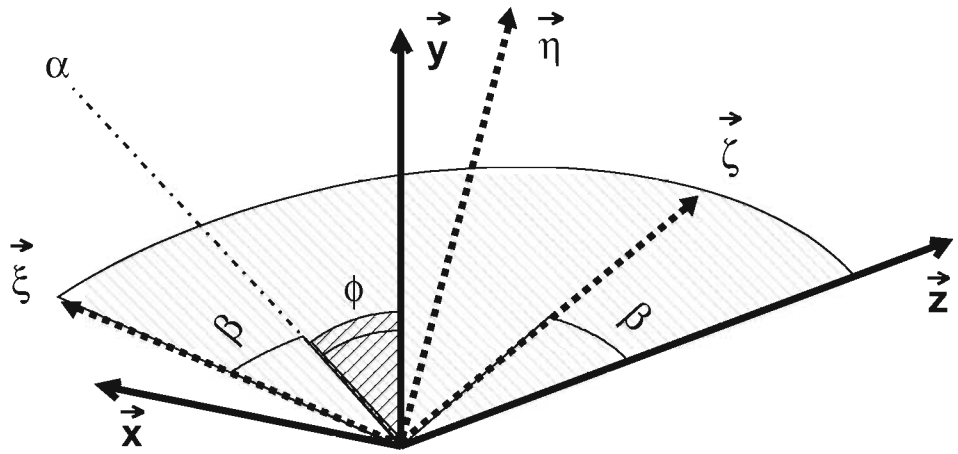

Figure 3.1: Rotation of the "internal" coordinate system $\xi\eta\zeta$ into the system of the Madison Convention xyz. The first Euler angle is 0°, the ζ-axis being the *vertical*. The second rotation is around the *line of nodes*, the η-axis, by -β°; it is negative, because the rotation is from ξ-axis to ζ-axis. It brings the ξ-axis in the x-y plane, the position shown as α. The final rotation is around the ζ-axis, the *figure axis*, which positions the η-axis along the y-axis. The corresponding angle is -(90-ϕ)°, again negative, because the rotation is clockwise in the ξ-ζ plane.

3.3 can be written in terms of p_ζ, $p_{\zeta\zeta}$ and the spin-symmetry axis direction angles, β and ϕ. It is more convenient to work with the spherical tensor and then go back to the Cartesian. The t_{kq} tensor can be obtained by rotational transformation of tensor τ_{kq} [Edm74],

$$t_{kq} = \sum_{q'=-k}^{k} \tau_{kq'} \mathfrak{D}^{(k)}_{q'q} \tag{3.4}$$

The matrix $\mathfrak{D}$ describes the rotation from the coordinate system of τ_{kq} to the system of t_{kq}. The Euler angles that define such a rotation are 0°, $-\beta$ and $-(90° - \phi)$, see Figure 3.1

Using this transformation, the beam tensor moments

$$\tau_{10} = \sqrt{\frac{3}{2}}\mathrm{p}_\zeta, \quad \tau_{20} = \frac{\mathrm{p}_{\zeta\zeta}}{\sqrt{2}} \tag{3.5}$$

are transformed into

$$\begin{aligned}
\mathrm{t}_{11} &= -\imath\tau_{10}\frac{\sin\beta e^{\imath\phi}}{\sqrt{2}} \\
\mathrm{t}_{20} &= \frac{\tau_{20}}{2}(3\cos^2\beta - 1) \\
\mathrm{t}_{21} &= -\imath\tau_{20}\sqrt{\frac{3}{2}}\sin\beta\cos\beta e^{\imath\phi} \\
\mathrm{t}_{22} &= -\tau_{20}\sqrt{\frac{3}{8}}\sin^2\beta e^{2\imath\phi}
\end{aligned} \tag{3.6}$$

By plugging the above expressions into Equation 3.2 and noting that

$$\begin{aligned}
i\mathrm{T}_{11} &= \frac{\sqrt{3}}{2}\mathrm{A}_y \\
\mathrm{T}_{20} &= \frac{\mathrm{A}_{zz}}{\sqrt{2}} \\
\mathrm{T}_{21} &= -\frac{1}{\sqrt{3}}\mathrm{A}_{xz} \\
\mathrm{T}_{22} &= \frac{1}{2\sqrt{3}}\Big(\mathrm{A}_{xx} - \mathrm{A}_{yy}\Big),
\end{aligned} \tag{3.7}$$

we get the following expression for the cross section:

$$\begin{aligned}
\sigma = \sigma_0\Big(1 + \sqrt{3}\mathrm{p}_\zeta i\mathrm{T}_{11}\sin\beta\cos\phi + \frac{1}{2\sqrt{2}}\mathrm{p}_{\zeta\zeta}\mathrm{T}_{20}(3\cos^2\beta - 1) + \\
\sqrt{3}\mathrm{p}_{\zeta\zeta}\mathrm{T}_{21}\sin\beta\cos\beta\sin\phi - \frac{\sqrt{3}}{2}\mathrm{p}_{\zeta\zeta}\mathrm{T}_{22}\sin^2\beta\cos 2\phi\Big)
\end{aligned} \tag{3.8}$$

or

$$\begin{aligned}
\sigma = \sigma_0\Big(1 + \frac{3}{2}\mathrm{p}_\zeta\mathrm{A}_y\sin\beta\cos\phi + \frac{1}{4}\mathrm{p}_{\zeta\zeta}\mathrm{A}_{zz}(3\cos^2\beta - 1) - \\
\mathrm{p}_{\zeta\zeta}\mathrm{A}_{xz}\sin\beta\cos\beta\sin\phi - \frac{1}{4}\mathrm{p}_{\zeta\zeta}(\mathrm{A}_{xx} - \mathrm{A}_{yy})\sin^2\beta\cos 2\phi\Big)
\end{aligned} \tag{3.9}$$

Appropriate choice of the beam polarization and the polarization axis alignment (i.e. β and ϕ) makes a measurement sensitive to the analyzing powers of interest.

To use the expression above for direct extraction of the analyzing powers, we need to know the cross section for the reaction initiated by unpolarized beam. In order to determine the cross section from the observed yields we need to know the detector efficiencies and solid angles, the target thickness, and the integrated beam current. In practice, multiple beam polarization states or identical detectors at opposite angles are used to construct ratios of the yields. This way, many factors such as detector efficiencies, solid angles and target thickness cancel out, greatly reducing systematic errors.

For the A_y measurements of this work we used a pure vector-polarized deuteron beam with the quantization axis set vertically, i.e. $\beta = 90°$, $\phi = 0°$. The beam was vector-polarized, having a finite p_ζ and zero $p_{\zeta\zeta}$, so the A_{yy} dependence was removed. In this case the yield observed with a detector positioned at angle θ is

$$Y(\theta) = Y_0(\theta)\left(1 + \frac{3}{2}p_\zeta A_y(\theta)\right) \tag{3.10}$$

where $Y_0(\theta)$is the yield with the unpolarized beam.

From the expression above we see that the vector analyzing power A_y characterizes the dependence of the cross section on the up-down vector beam polarization, and non-zero $A_y(\theta)$ results in left-right asymmetry. It can be shown from the following consideration. For a vector-polarized beam of some p_ζ, yield measured by a detector positioned on the left of the beam (positive x-direction of the Madison system) is

$$Y_L = Y_0(\theta)\left(1 + \frac{3}{2}p_\zeta A_y(\theta)\right) \tag{3.11}$$

The yield for a detector positioned symmetrically on the right would be

$$Y_R = Y_0(\theta)\left(1 + \frac{3}{2}\mathrm{p}_\zeta \mathrm{A}_y(-\theta)\right) \tag{3.12}$$

But if we rotate the beam line by 180°about its axis, the "right" detector will be in the position of the "left" one, but would observe the yield from beam of negative polarization -p_ζ:

$$Y_R = Y_0(\theta)\left(1 - \frac{3}{2}\mathrm{p}_\zeta \mathrm{A}_y(\theta)\right) \tag{3.13}$$

The vector analyzing power A_y characterizes the dependence of the cross section on the "vertical" beam polarization. By combining Equation 3.11 and Equation 3.13, we obtain

$$\mathrm{A}_y(\theta) = \frac{2}{3\mathrm{p}_\zeta}\frac{Y_L - Y_R}{Y_L + Y_R}. \tag{3.14}$$

In our measurements we were not able to set up two identical detectors for $+\theta$ and $-\theta$, so we used two beam polarization states to perform a measurement at angle θ. Having the deuterons switching between two states of p_ζ, we find the expression for $\mathrm{A}_y(\theta)$:

$$\mathrm{A}_y(\theta) = \frac{2}{3}\frac{Y_1 - Y_2}{Y_2\mathrm{p}_{\zeta_1} - Y_1\mathrm{p}_{\zeta_2}}. \tag{3.15}$$

For the first spin state we used transition $1 \leftrightarrow 4$ with the theoretical values of $\mathrm{p}_\zeta = -2/3$ and $\mathrm{p}_{\zeta\zeta} = 0$. The second spin state utilized transition $3 \leftrightarrow 6$ with the theoretical values of $\mathrm{p}_\zeta = +2/3$ and $\mathrm{p}_{\zeta\zeta} = 0$. The actual values of p_ζ were about 75% of the maximum achievable numbers, with 7% systematic error on the measured values. The values of $\mathrm{p}_{\zeta\zeta}$ were set to zero, within uncertainty of 7% (i.e. $\mathrm{p}_{\zeta\zeta} = 0 \pm 0.07$).

The measurements of the tensor analyzing power $\mathrm{T}_{20}(\theta)$ were made in a similar way. The yield is sensitive to T_{20} when the beam quantization axis is set along the

beam momentum, i.e. $\beta = 0°$ and $\phi = 0°$. The expression for the yield is

$$Y(\theta) = Y_0(\theta)\left(1 + \frac{1}{\sqrt{2}} p_{\zeta\zeta} T_{20}\right) \tag{3.16}$$

If two states of $p_{\zeta\zeta}$ are used, the resulting expression for the tensor analyzing power is:

$$T_{20}(\theta) = \sqrt{2}\frac{Y_1 - Y_2}{Y_2 p_{\zeta\zeta_1} - Y_1 p_{\zeta\zeta_2}} \tag{3.17}$$

The tensor analyzing power T_{20} is a measure of how the cross section depends upon the m-state of the deuteron ($m = 0$ compared to $m = \pm 1$) when the beam polarization is along the momentum direction. With the beam polarized along the momentum axis the resulting asymmetry does not have azimuthal dependence, i.e. there is no left-right asymmetry. For the first spin state we used the $2 \leftrightarrow 4$ transition providing $p_{\zeta\zeta} = -1$, $p_\zeta = +1/3$, and for the second spin state $3 \leftrightarrow 5$, with $p_{\zeta\zeta} = +1$, $p_\zeta = -1/3$. The values of $p_{\zeta\zeta}$ and p_ζ were around 70% to 85% of the maximum achievable values and also had 7% systematic error.

The errors in the values of the analyzing power at every angle include systematic errors in the detector position, error in the polarization values, and the errors in the γ-ray peak yield extraction, including the statistical errors and systematic errors of the peak fitting. The error propagation and numerical evaluation of the errors is performed in Chapter 4, Section 4.4.

The measured angular distributions of the analyzing powers can be expanded in terms of Legendre and associated Legendre polynomials, see Section 3.2 below for details. For example, the unpolarized reaction cross section can be written as

$$\sigma_0(\theta) = \sum_k A_k P_k(\cos\theta),$$

and the vector analyzing power $A_y$as

$$A_y(\theta) = \frac{2}{3}\frac{\sum_k B_k P_k^1(\cos\theta)}{\sum_{k'} A_{k'} P_{k'}(\cos\theta)},$$

where P_k and P_k^1 are Legendre and the first order associated Legendre polynomials.

The expansion coefficients (i.e. A_k and B_k above) can be related to the transition matrix elements involved in the reaction [Sey79]. The fits of the measured angular distributions of the polarization observables to the Legendre polynomials result in values of amplitudes and relative phases of the transition matrix elements. This is the method of the TME analysis performed on the data. The analysis will be considered in depth in Chapter 5. Here we will discuss the details of angular momentum coupling and the transition matrix elements involved in the $^2H(\vec{d},\gamma)^4He$ reaction at low energies.

3.2 Channel Spin Coupling Scheme

Let us consider a γ-ray-capture reaction in form of

$$\boldsymbol{a}(\boldsymbol{x},\mathcal{L})\boldsymbol{c},$$

where $\boldsymbol{a}$ is the spin of the target nucleus, $\boldsymbol{x}$ is the spin of the projectile with relative orbital angular momentum of $\boldsymbol{l}$, $\boldsymbol{\mathcal{L}}$ is the multipolarity of the outgoing γ-ray, and $\boldsymbol{c}$ is the spin of the residual nucleus after the gamma emission. The complex TME is defined as

$$R = \langle \Psi_f | \widehat{H} | \Psi_i \rangle,$$

where Ψ_i and Ψ_f are the initial and final state wave functions and $\widehat{H}$ is the interaction Hamiltonian of the transition. Each matrix element is identified by its quantum

numbers in the channel spin coupling scheme. In this scheme, spins of the projectile and target, $\boldsymbol{a}$ and $\boldsymbol{x}$, are coupled first to give the channel spin $\boldsymbol{s}$. The channel spin is then combined with the projectile angular momentum $\boldsymbol{l}$ to form the total angular momentum $\boldsymbol{j}$ of the γ-ray-emitting nucleus. These quantum numbers $\boldsymbol{j}$, $\boldsymbol{l}$, $\boldsymbol{s}$, and multipolarity $\mathcal{L}$ and the mode (electric or magnetic, labeled by p) of the transition, can be used to label every TME. The $\boldsymbol{j}$, $\boldsymbol{l}$, and $\boldsymbol{s}$ quantum numbers label the initial wave function, while the multipolarity and mode ($\mathcal{L}$ and p) of the γ-ray describe the electromagnetic transition to the final state. Every TME can be written in terms of its amplitude and its phase

$$R(\boldsymbol{j},\boldsymbol{l},\boldsymbol{s},\mathcal{L}p) = |\mathrm{R}(\boldsymbol{j},\boldsymbol{l},\boldsymbol{s},\mathcal{L}p)|\exp(\imath\phi_{\boldsymbol{j},\boldsymbol{l},\boldsymbol{s},\mathcal{L}p}).$$

In general, for a beam of arbitrary spin polarized with moments of rank ≤ 2, the radiative capture reaction cross section can be written as:

$$\sigma(\theta,\phi) = \sum_k (\mathrm{A}_k\mathrm{P}_k(\cos\theta) + \mathrm{B}_k\mathrm{P}^1_k(\cos\theta)\mathrm{p}_y + \mathrm{C}_k\mathrm{P}_k(\cos\theta)\mathrm{t}_{20} + \mathrm{D}_k\mathrm{P}^1_k(\cos\theta)\Re(\mathrm{t}_{21}) + \mathrm{E}_k\mathrm{P}^2_k(\cos\theta)\Re(\mathrm{t}_{22})), \quad (3.18)$$

where $\Re$ designates the real part. The analyzing powers can be expressed in terms of these expansion coefficients by comparing Equation 3.18 and Equation 3.2 or Equation 3.3. For example,

$$\sigma_0(\theta)\frac{3}{2}\mathrm{A}_y(\theta) = \sum_k \mathrm{B}_k\mathrm{P}^1_k(\cos\theta);$$

the unpolarized cross section angular distribution can be expressed via Legendre polynomials $\mathrm{P}_k(\cos\theta)$:

$$\sigma_0(\theta) = \sum_k \mathrm{A}_k\mathrm{P}_k(\cos\theta), \quad (3.19)$$

so that the analyzing power can be written as:

$$\mathrm{A}_y(\theta) = \frac{2}{3}\frac{\sum_k \mathrm{B}_k\mathrm{P}^1_k(\cos\theta)}{\sum_{k'} \mathrm{A}_{k'}\mathrm{P}_{k'}(\cos\theta)}. \quad (3.20)$$

In a similar way,

$$T_{20}(\theta) = \frac{\sum_k C_k P_k(\cos\theta)}{\sum_{k'} A_{k'} P_{k'}(\cos\theta)}. \tag{3.21}$$

According to the formalism of [Sey79], the Legendre expansion coefficients A_k, B_k and C_k can be written in terms of the transition matrix elements $R(\boldsymbol{j}, \boldsymbol{l}, \boldsymbol{s}, \mathcal{L}p)$ described above.

The channel-spin coupling scheme is not the only way to relate the angular distributions with the matrix elements involved in the reaction. An alternative scheme is the jj coupling scheme. According to this scheme, orbital angular momentum and spin are coupled to total angular momentum of the projectile and the target, j; then the projectile and the target angular momenta are coupled to form the total angular momentum of the channel. The observables can also be written in terms of the matrix elements in this scheme.

The last step necessary to relate the observable angular distributions to the TMEs is to consider which matrix elements should be taken into account for the reaction in the energy region of interest.

3.3 Transitions Involved in the Reaction

The d-d cluster model representation of ^{4}He describes the ground state of the alpha particle as a superposition of two states in which the spins of the deuterons are coupled to the total spin $\boldsymbol{S}$ and have relative orbital angular momentum of $\boldsymbol{L}$. We can write the ground state as a sum of $^1S_0$ (using $^{2S+1}L_J$ notation) and $^5D_0$ states. The bound states are coupled to the continuum states via electromagnetic transitions.

The reacting deuterons of the entrance channel are considered in the channel spin coupling scheme, having orbital angular momentum $\boldsymbol{l}$ and total spin $\boldsymbol{s}$. The presence of two identical bosons in the entrance channel sets conditions on the values of $\boldsymbol{l}$ and $\boldsymbol{s}$. The requirement that the total wave function be symmetric means that the value of $\boldsymbol{l}+\boldsymbol{s}$ should be even. Thus, for electromagnetic radiation of multipolarity ≤ 2, all of the allowed transitions are:

- (E1, $^3p_1$), (M1, $^5d_1$)
- (E2, $^1d_2$), (E2, $^5s_2$), (E2, $^5d_2$), (E2, $^5g_2$)
- (M2, $^3p_2$), (M2, $^3f_2$)

Something can be said about the expected relative strength of these TMEs. The higher angular momentum capture waves will be suppressed by penetrability arguments. In general, higher order multipoles (E2 and M2) should be suppressed with respect to the lower order ones (E1 and M1). The electric multipoles are stronger than the magnetic ones of the same order. However, in the present situation one would expect the p-wave E1 capture to be suppressed, because the transition involves spin-flip ($\Delta S = 1$), and at our energies, the $\Delta S = 1$ part of the electric dipole operator is about 1 % of the "normal" $\Delta S = 0$ E1 operator. Furthermore, E1 radiation is suppressed by the isospin selection rules. Sine the deuteron has $T = 0$, the entrance channel isospin is zero. The ground state of ^{4}He has $T = 0$. Therefore transition will be isoscalar ($\Delta T = 0$), but $\Delta T = 0$ E1 transitions are suppressed in self-conjugate nuclei [Wil69]. The M1 radiation is suppressed as well, so the E2 radiation is expected to dominate. However, it has been shown that non-E2 transitions should be considered (see notes below). Still, having only a small amount of experimental data, we need to reduce the set of TMEs used to fit the measured angular distributions.

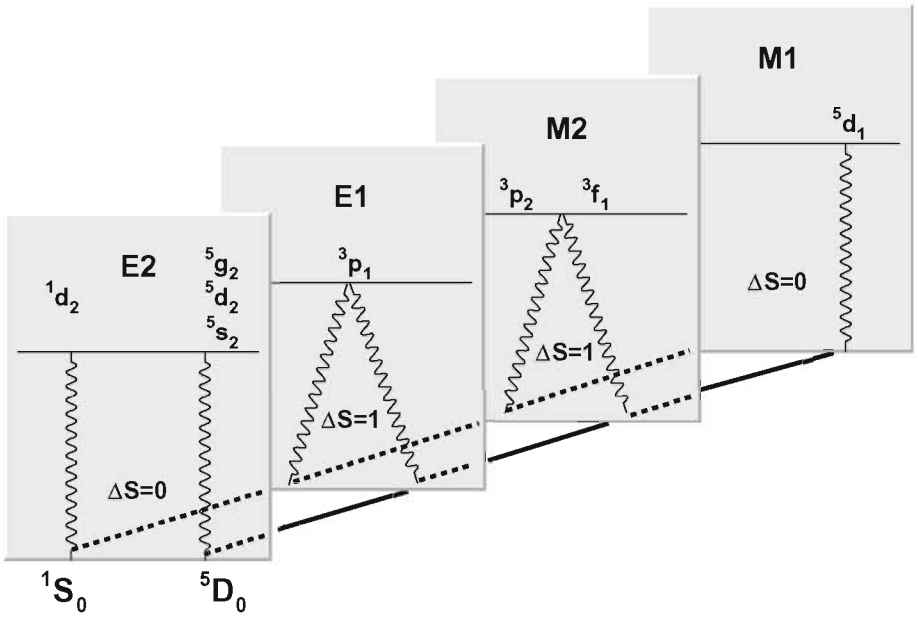

Figure 3.2: Electromagnetic transitions from scattering states of two deuterons to the ground state of ^{4}He. The alpha-particle ground state, $J^\pi = 0^+$, T=0, is considered as combination of dominating $^1S_0$ (L=0, S=0) state with $^5D_0$ (L=2, S=2) state admixture. The spin-isospin selection rules help us in estimation of the relative transition strength.

The decision is made based on what we mentioned above and on the TME analysis of the previous experimental data.

We can simplify our calculations if we neglect the high angular momentum partial waves. The $\boldsymbol{l} = 3$ $^3f_2$ M2 matrix element should be small compared to the M2 $^3p_2$ term with $\boldsymbol{l} = 1$. Also, of the E2 transitions, we can safely discard the $^5g_2$, $\boldsymbol{l} = 4$ term.

Let us consider the matrix elements producing E2 radiation. The $^1d_2$ and $^5d_2$ partial waves are dominant at energies above 10 MeV, accounting for 80% to 90% of the total capture strength [Mel86], [Lan89]. As we go down in energy from 10 to 1 MeV, the total E2 strength diminishes but is still significant, accounting for more than 40% [Lan88],[Lan89]. Among the E2 transitions the amplitude of the $^1d_2$ term becomes dominant, as the beam energy is reduced from 10 to 1 MeV. This can be explained by the capture to S- and D-states of ^{4}He: the $^1d_2$ partial wave is captured to the S-state, the predominant part of the ^{4}He ground state wave function, while the $^5s_2$ and $^5d_2$ waves are captured to the small D-state. At energies below 1 MeV, assuming only E2 radiation, the $^5s_2$ term would be expected to dominate due to the centrifugal barrier effect.

However, there is evidence of non-E2 multipoles involved in the reaction, at the level of 10 – 20%, even at 10 MeV. At lower energies their contribution is found to be even more significant. In the vicinity of 100 keV d-waves are suppressed by a factor of 100 compared to p-waves on the basis of penetrability considerations. This would leave only three partial amplitudes to be considered: E2 $^5s_2$, E1 $^3p_1$, and M2 $^3p_2$. The transition matrix element analysis including these partial waves for E_d=80 keV resulted in solutions with a total p-wave capture strength of 50% to 85% of the total capture strength [Kra92]. A similar analysis, including only s- and p-waves, was

performed on our data set. The results of this analysis produced a unique solution, as will be discussed in Chapter 5, indicating that the reaction proceeds via almost equal strength s-wave and p-wave capture channels, with $^5s_2$ term accounting for 55% of the total capture strength, with $^3p_1$ and $^3p_2$ terms of 29% and 16% respectively.

3.4 From Angular Distributions to TMEs

The set of the transition matrix elements included in the analysis defines the Legendre polynomial expansion coefficients A_k, B_k, C_k, D_k, and E_k [Sey79]. A FORTRAN code LSCOEF was used to express each of the above coefficients as a sum of products of a numerical coefficient, two TME amplitudes, and a cosine (or sine in the case of B_k) of the phase difference of the TMEs. Then, the observables (the differential cross section, and vector and tensor analyzing powers) are constructed as functions of angle θ ($\cos(\theta)$ being the argument of the Legendre polynomials), see Equation 3.20 and Equation 3.21 as examples. The polarization observable expressions written like this depend on a set of parameters, the TME amplitudes and relative phases. In our case we considered three TMEs, i.e. there are three amplitudes and two relative phases (with respect to one of the phases, $^5s_2$, which is fixed to zero), resulting in a total of five parameters.

Because of the finite size of the detectors, we used the "finite geometry coefficients", Q_k [Fer65]. The Q-coefficients depend on size of the detector and distance to the target; the coefficients enter in the expressions for the observables as prefactors for the Legendre expansion coefficients.

It was more convenient to write the amplitudes of the TMEs not in absolute values, but as percentage of the total capture strength. The two quantities can be

related by using the value of the A_0 coefficient. The total absolute cross section for unpolarized beam can be found by integration of Equation 3.19 over solid angle:

$$\sigma_{total} = \int \sigma(\theta) do = 4\pi A_0 \tag{3.22}$$

The expression for A_0, following [Sey79], is

$$A_0 = \sum_t (2j_t + 1)|R_t|^2, \tag{3.23}$$

where j is the total angular momentum of the γ-ray-emitting nucleus, and $|R|$ is the absolute magnitude of the correspoding transition matrix element. So the relative amplitude of transition t is given by $(2j_t+1)|R_t|^2/A_0$. In our analysis we started with relative amplitudes, from which we could calculate the absolute TME values, $|R_t|^2$. Then, the Legendre polynomial expansion coefficients were constructed. After the fit (described below), the final $|R_t|^2$ values werw used to calculate the resulting relative strengths of the transition matrix elements.

The final step is to optimize the parameters (the amplitudes and the relative phases) to obtain expressions for the observables that describe the measured data set the best. This has been done by constructing a least square, χ^2 function, as the sum of the χ^2 for every observable (e.g. $\chi^2_{\mathrm{A}_y} = \sum_i \left(\frac{F_{\mathrm{A}_y}(\theta_i) - \mathrm{A}_y(\theta_i)}{\Delta \mathrm{A}_y(\theta_i)}\right)^2$, where $\mathrm{A}_y(\theta_i)$ and $\Delta\mathrm{A}_y(\theta_i)$ are the measured analyzing powers and their errors, and $F_{\mathrm{A}_y}(\theta)$ is the expression of $\mathrm{A}_y(\theta)$ via the Legendre polynomials) and by performing a least-square minimization procedure on all of the data points. The minimization routine calls the standard package MINUIT [Jam71], and is available as a FORTRAN code on the TUNL VAX cluster, or as a C++ code, utilizing the built-in class TMinuit of the data analysis package ROOT.

The details of the execution, results, and discussion of the TME extraction from the observable angular distributions will be given in Chapter 5.

Chapter 4

Data Analysis

All the incoming data was written into histograms using XSYS sorting routines EVAL. ADC signals were sorted according to spin state bits and shield coincidence veto bits.

4.1 Sorting

In XSYS one needs to provide configuration files describing which CAMAC module would produce a "look-at-me" (LAM) signal, what other CAMAC modules would be read out whenever the LAM is set, and what channels of the modules are to be read out. This information is given in Data Acquisition Program (DAP) files. All the spectra definitions, event formats, and the sorting algorithms are given in the event analysis files, written in Event Analysis Language (EVAL). In our case we typically read two channels of one ADC as the energy signals of two NaI(Tl) detectors, and one channel of another ADC for the spectrum from a solid-state silicon detector, used for

target monitoring. All the signals were sorted into multiple spectra according to the spin-bit set by feedback from the ABPIS. Events with spin-veto bit set (a short period when the spin direction is flipped) were rejected. For NaI(Tl) detector signals the shield-veto bit defined whether the event was directed into a "good" spectrum (bit not set, no coincidence of NaI(Tl) with the shield) or a "vetoed" spectrum (cosmic ray event, or γ-ray did not deposit its full energy in the crystal). The "good" spectra were used to extract asymmetry in the capture peak for the two spin states.

4.2 Data Analysis Software

All data analysis was performed using the Object-Oriented Toolkit *ROOT* from CERN (`http://root.cern.ch`). The package provides a multitude of precompiled classes for data storage, manipulation, and display, as well as physics and mathematics classes. Implementation of user-defined classes, functions, and so on is also very straightforward. The XSYS data files were read directly into ROOT-histograms, which were manipulated later using C-based scripts: ROOT-macros. Also, ROOT has a built-in class based on the well-known MINUIT minimization package, which allows us to fit data with precompiled or user-defined functions and have very good control and feedback on the minimization routine.

4.3 Spectra Fitting

In analyzing power measurements, an extra care should be taken to avoid false asymmetries. The first step in the spectra analysis was to check if we had equal amounts of beam in both spin states. This was made by comparing the spin-state

scalers, as well as by integrating the very high energy part of the histograms, which contains constant-rate cosmic ray background.

The background and the peak fits were made starting with the spectrum containing both spin states to have better statistics and to get more reliable fits. The total fit consisted of the 23.8 MeV γ-ray detector response function superimposed on a continuous background.

The background is described well by an exponential with a quadratic argument:

$$\exp(p_0 + p_1 E + p_2 E^2) \tag{4.1}$$

where E is the energy and p_0, p_1, and p_2 are the parameters obtained with the fit in the region above the capture peak.

The response function was obtained by fitting the parametrized line-shape, which is a composite function of two exponentials with arguments of forth-order polynomials ([Bal92]):

$$F_{resp}(E) = \exp(a_1 + b_1 E + c_1 E^2 + d_1 E^3 + e_1 E^4) \tag{4.2}$$

for $E < E_j$, and

$$F_{resp}(E) = \exp(a_2 + b_2 E + c_2 E^2 + d_2 E^3 + e_2 E^4) \tag{4.3}$$

for $E > E_j$, where E is the γ-ray energy, E_j is the matching point of the exponentials, and $a_1, a_2, b_1, b_2, c_1, c_2, d_1, d_2, e_1$, and e_2 are the parameters obtained by fitting a NaI(Tl) detector response function to a mono-energetic γ-ray beam. This had been previously done using the ^{3}H(p,γ)^{4}He reaction (Q = 19.8 MeV) with 5.4 MeV protons which produce 23.8 MeV capture γ-rays. A detector similar to those used in the current experiment, a tritiated-titanium target, and protons accelerated by the tandem accelerator at TUNL were utilized [Kra92]. The fit was performed in the energy

a_1	-10149.542
b_1	1883.5661
c_1	-130.90048
d_1	4.0382005
e_1	-0.046645767
a_2	306021.28
b_2	-48598.524
c_2	2894.1017
d_2	-76.593899
e_2	0.76009464
E_j	24.39899
E_{low}	21.400
E_{high}	26.000

Table 4.1: NaI(Tl) detector response function fit parameters. The corresponding line-shape is shown in the Figure 4.1. The high precision of the response function coefficients is necessary to obtain finite values of the response function.

region E_{low} to E_{high}, as shown in Figure 4.1. For the energies higher than E_{high}, the response function is set to zero, and for the energies below E_{low}, the function was linearly extrapolated, with the function and its derivative being continuous at E_{low}. The results of the fit and all the parameters are given in the Table 4.1.

The parametrized response function used to fit the capture peak included three parameters, height, width, and centroid of the line-shape function, to accommodate the differences between the detector used to obtain the response function and the one used in the present $^2\mathrm{H}(\vec{d},\gamma)^4\mathrm{He}$ measurements. So, the final response function of the detector used to fit the peak was given by the function

$$F_{peak}(E') = height \cdot \exp(a_1 + b_1 E' + c_1 E'^2 + d_1 E'^3 + e_1 E'^4) \tag{4.4}$$

for $E' < E_j$, and by the function

$$F_{peak}(E') = height \cdot \exp(a_2 + b_2 E' + c_2 E'^2 + d_2 E'^3 + e_2 E'^4) \tag{4.5}$$

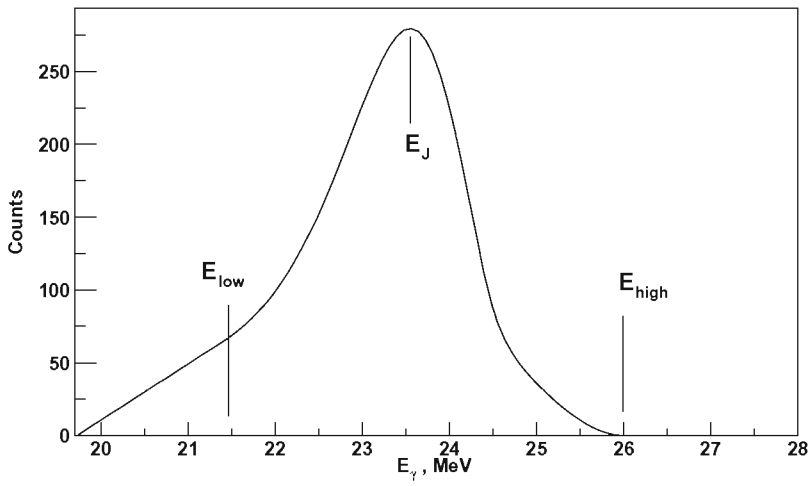

Figure 4.1: NaI(Tl) detector response function used for spectra fitting. The functional expression is given in the text. The parameter values are in the Table 4.1

for $E' > E_j$, where $E' = \frac{(E-centr)}{width} + E_j$. All the parameters in the exponential and the definition of E_j are the same as previously defined for the response function in Equation 4.2 and Equation 4.3.

A χ^2minimization procedure was applied to the spectra of combined spin states, with the fitting parameters of p_0, p_1, and p_2 for the background function defined by Equation 4.1 and $centr, width$, and $height$ for the peak given by Equation 4.4 and Equation 4.5. The fit region enclosed the capture peak, but special care was taken to ascertain that we didn't move too close to the threshold where pile-up might have distorted the shape of the background. In a good fit the background function, extrapolated to the lower boundary of the fit region, and the detector response lineshape do not cross but come to the same value.

After fitting the combined spin state spectrum, the background function was scaled down by a factor of two (by changing the p_0 parameter accordingly) to represent

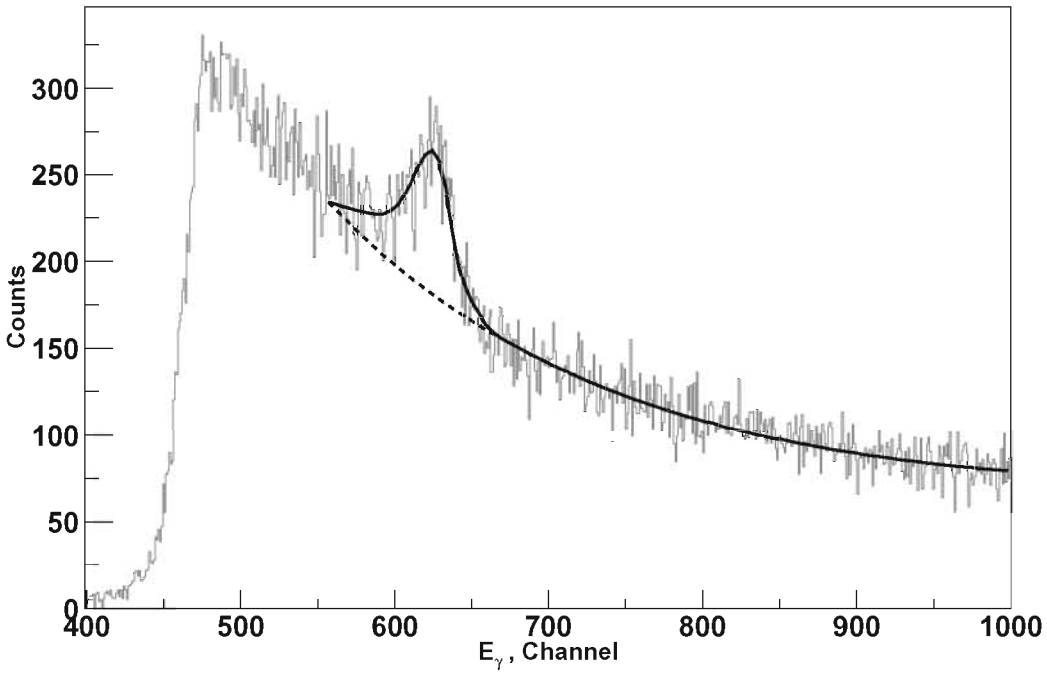

Figure 4.2: A typical spectrum used to obtain the capture γ-ray-yields. The NaI(Tl) detector line-shape (shown in Figure 4.1) and the background function (given by Equation 4.1) are fitted simultaneously. The yield is calculated as the difference of the total fit (line-shape and the background, solid curve) and the background (dashed curve).

the background in a single spin state. The background fit parameters were fixed at this point. Also, the peak position (given by *centr* of the line-shape function) and the peak width (*width* parameter) were fixed while fitting the single spin states. The only free parameter was the peak height (*height*). The difference in this parameter for the two spin states defined the asymmetry. The yield of the capture γ-rays was calculated as the integral of the response function over the fitting region.

4.4 Errors and Corrections

To calculate the values of the analyzing powers, we used the expressions derived in Section 3.1, such as Equation 3.15 and Equation 3.17. Possible sources of errors in analyzing power calculations are errors in the beam polarization values and in the measured capture γ-ray yields. The errors in the yields have statistical and systematic contributions, the latter being the result of our spectrum fitting method. A number of different fitting procedures were performed to confirm that these systematic errors are less significant than the statistical errors.

As was noted in the previous section, the fit quality depends on the fit region; the initial values used for the parameters can also affect the fit quality. So the first step in analysis of every spectrum was to make sure that the fit does not extend too close to the threshold region and that the initial parameters, even when varied by 5 – 10%, still provide a reasonable fit. The fit procedure is described in Section 4.3, and the fit is performed using the MIGRAD minimizer, which is part of ROOT class TMinuit. The minimization routine displays the χ^2 for the fit and the parameter values, step size, and errors. Typically, we had about 1000 counts in our capture peak, and the minimizer was able to locate the peak and fit the background well, resulting in the

final χ^2_ν for the spectrum fit to be rather close to 1. To explore the impact of the errors in the parameters on the calculated yield values, we used the following procedure. A fit was performed and the optimal parameter values were obtained. Typical errors in *height* and *width* parameters were 5%; in the peak position, *centr*, 0.1%; the error in p_0 was about 0.5%, and errors in p_1 and p_2, the background fit parameters were close to 2%. Then, all but one of the parameters were fixed while one of them was varied by the error value, and then the yield was calculated in the usual way, by integrating the line-shape function. It was found that the resulting difference in the γ-ray yield was 2 to 4 % of the "optimal fit" yield. It is less than the statistical error of the number of counts in the peak, and less than the dominant error, the uncertainty of the beam polarization value, estimated to be close to 7%.

To find the final errors in the values of analyzing powers, we used the propagation of errors method, see, for example [Bev69].

With the vector analyzing power A_y given by Equation 3.15, we obtain the following expression for the error, ΔA_y:

$$\Big(\Delta A_y(\theta)\Big)^2 = \Big(\frac{A_y(\theta)}{Y_1(\theta)p_{\zeta_2} - Y_2(\theta)p_{\zeta_1}}\Big)^2 \Big(\big(\Delta p_{\zeta_1} Y_2(\theta)\big)^2 + \big(\Delta p_{\zeta_2} Y_1(\theta)\big)^2 + Y_1(\theta)Y_2(\theta)\big(Y_1(\theta)+Y_2(\theta)\big)\frac{\big(p_{\zeta_1}-p_{\zeta_2}\big)^2}{\big(Y_1(\theta)-Y_2(\theta)\big)^2}\Big). \quad (4.6)$$

The expressions for the tensor analyzing power T_{20} are very similar; the analyzing power is also written as an asymmetry, see Equation 3.17 (except now we use $p_{\zeta\zeta}$,

not p_ζ). The expression for the error, ΔT_{20}:

$$\Big(\Delta T_{20}(\theta)\Big)^2 = \Big(\frac{T_{20}(\theta)}{Y_1(\theta)p_{\zeta\zeta_2} - Y_2(\theta)p_{\zeta\zeta_1}}\Big)^2 \Big(\big(\Delta p_{\zeta\zeta_1} Y_2(\theta)\big)^2 + \big(\Delta p_{\zeta\zeta_2} Y_1(\theta)\big)^2 + Y_1(\theta)Y_2(\theta)\big(Y_1(\theta) + Y_2(\theta)\big)\frac{\big(p_{\zeta\zeta_1} - p_{\zeta\zeta_2}\big)^2}{\big(Y_1(\theta) - Y_2(\theta)\big)^2}\Big). \quad (4.7)$$

In the expressions above, we used the fact that the error in the yield value is mostly statistical, i.e. $\Delta Y(\theta) = \sqrt{Y(\theta)}$. The uncertainties in the beam polarization are Δp_ζ (for A_y) and $\Delta p_{\zeta\zeta}$(for T_{20}), which were set to be 7% of the polarization values p_ζ and $p_{\zeta\zeta}$ during a particular run.

4.5 Observed Angular Distributions of Analyzing Powers

The capture γ-ray yields obtained from the spectra were used to construct angular distributions of the analyzing powers.

Most of the data were taken with a beam energy of 115 keV. The 80-keV deuterium ions out of the polarized source were stopped in the ice target, which was held at a potential of -35 kV. We obtained angular distribution data for the analyzing powers A_y and T_{20}. Table 4.2 and Table 4.3 summarize our measurements at this beam energy and contain the position of the detectors, the yields in the two spin states, the beam polarization values, and the calculated observables.

To cross check our data with the 80-keV data obtained previously in TUNL, [Kra92], a few runs were made with a beam energy of 80 keV, providing some data for $T_{20}(\theta)$; the summary is given in Table 4.4.

Angle, θ_{la}	Y_1	Y_2	p_{ζ_1}	p_{ζ_2}	$A_y(\theta) \pm \Delta A_y(\theta)$
90°	301	559	-0.60	0.48	0.35 ± 0.04
90°	453	899	-0.60	0.49	0.47 ± 0.08
90°	516	942	-0.62	0.49	0.34 ± 0.04
132°	1810	989	-0.56	0.48	0.39 ± 0.04

Table 4.2: Data for $A_y(\theta)$, E_d=115keV. The asymmetry $(Y_1 - Y_2)$ for the 132°point has different sign, because the detector was placed to the right from the target.

Angle, θ_{lab}	Y_1	Y_2	$p_{\zeta\zeta_1}$	$p_{\zeta\zeta_2}$	$T_{20}(\theta) \pm \Delta T_{20}(\theta)$
39°	1997	2358	0.89	-0.89	-0.13 ± 0.04
53°	1625	2106	0.88	-0.89	-0.21 ± 0.04
123°	1756	1537	0.89	-0.89	0.11 ± 0.04

Table 4.3: Data for $T_{20}(\theta)$, E_d=115keV.

Angle, θ_{lab}	Y_1	Y_2	$p_{\zeta\zeta_1}$	$p_{\zeta\zeta_2}$	$T_{20}(\theta) \pm \Delta T_{20}(\theta)$
28°	645	452	0.87	-0.62	0.25 ± 0.14
58°	140	138	0.87	-0.62	0.00 ± 0.14

Table 4.4: Data for $T_{20}(\theta)$, E_d=80keV.

The errors in the observable values were calculated as described in the Section 4.4, and represent the statistical uncertainty in the yield values along with the systematic uncertainty in the beam polarization.

The data are shown in Figure 4.3 and Figure 4.4.

Our measurements did not include the differential cross section. With the high voltage applied to the target chamber it is impossible to get a direct reading of the integrated beam current (BCI) off the target. The target thickness is changing with time. These factors make the absolute cross section measurements very challenging. However, our experimental setup can be readily used for the cross section measurements. The solid state silicon detector, which was used to monitor the target quality, can be utilized to obtain the product of the beam current and the target thickness. Knowing the ^{2}H(d, p)^{3}H reaction cross section, (d, p) to (d, γ) branching ratio, stopping powers, detector efficiencies and geometries, one could calculate the differential cross section.

To compare our finite geometry data with the results of calculations, we need to find values of the analyzing powers for point geometry. The standard method is to perform a TME fit on the data with the finite geometry corrections, the Q-coefficients. Then, set all the Q-coefficients to 1 (corresponding to point-geometry), and calculate the analyzing powers based on the TMEs found before. The transition matrix elements analysis was performed on the data as described in Chapter 5. The following Q-coefficients were used: 1.0, 0.95821, 0.87827, 0.76705, and 0.63386. The corrected values are presented in Table 4.5.

One more step that has to be done to compare the measured values with calculations is to take into account stopping of the beam in our target. The observables that we obtain are integrated over the incoming deuteron energies E_d= 115 keV to 0

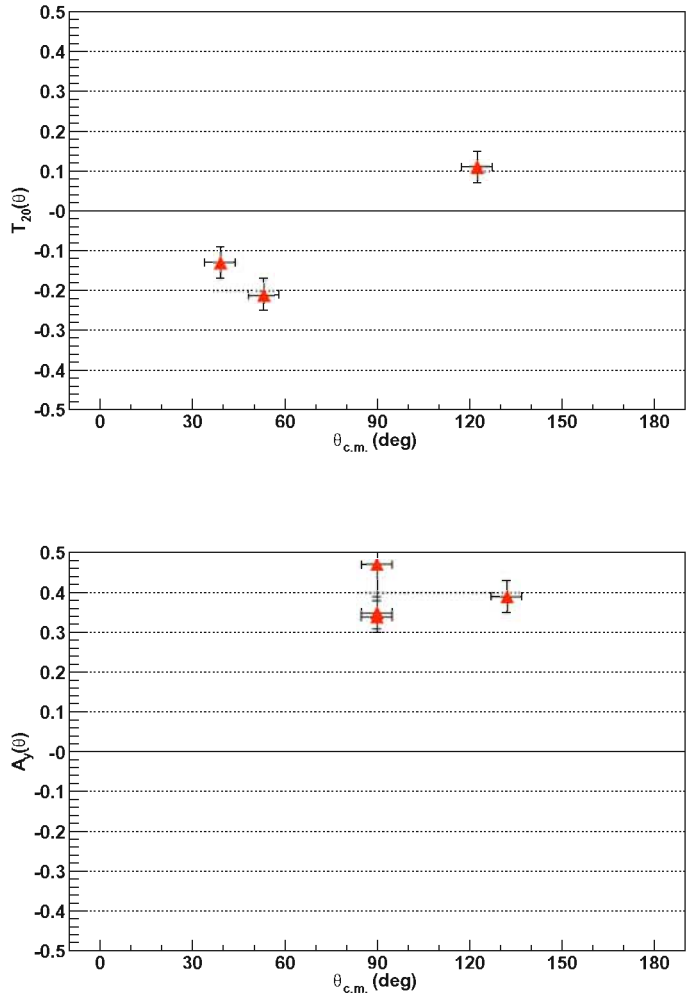

Figure 4.3: Data points for $A_y(\theta)$ and $T_{20}(\theta)$ beam energy of E_d=115keV.

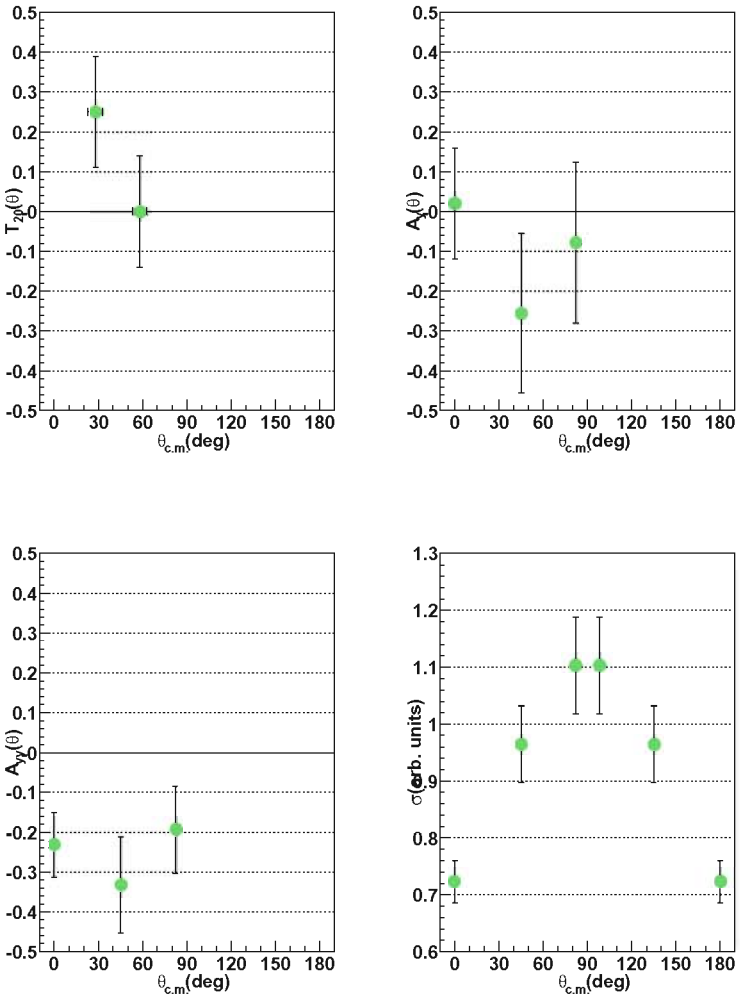

Figure 4.4: Data points from the previous measurements of ^{2}H($\vec{d},\gamma$)^{4}He reaction at E$_d$=80keV(differential cross section, A$_y$ and A$_{yy}$). Our measurement expand the data set for this energy by including T$_{20}$.

Angle, θ_{lab}	Observable	Measured	Corrected
39°	T_{20}	-0.13 ± 0.04	-0.12 ± 0.04
53°	T_{20}	-0.21 ± 0.04	-0.19 ± 0.04
123°	T_{20}	+0.11 ± 0.04	+0.11 ± 0.04
90°	A_y	+0.39 ± 0.03	+0.32 ± 0.03
132°	A_y	+0.39 ± 0.04	+0.38 ± 0.04

Table 4.5: Finite geometry corrected data for E_d=115keV.

keV.

A typical way to take the stopping beam in the target into account is to refer the measured observables to "effective", or "mean" energy. The mean energy is defined as the energy at which half of the total yield of the reaction is produced. As the beam penetrates the target by distance dx, we can calculate the change in the energy by using known stopping powers, $dE = \frac{dE}{dx}dx = -STP(E)dx$, where $STP(E) = -\frac{dE}{dx}(E)$ is the stopping power for the projectile ions in the target medium. For every slice dx, the reaction cross section $\sigma(E)$ is calculated. The yield from the beam that penetrated to position x_c where its energy is reduced from E_{beam} to E_c would be

$$Y_c = \int_{E_{beam}}^{E_c} \sigma(E) \frac{1}{STP(E)} dE \tag{4.8}$$

The above integral is calculated for E_c ranging from E_{beam} to 0, i.e. until the beam is stopped. The current yield (Y_c) is normalized to the total yield (integration from E_{beam} to 0), and the mean energy would be the one at which Y_c=1/2 Y_{total}.

For the described procedure we need to know the stopping power of deuterons in our target, and the reaction cross section as function of energy. The energy dependence of $STP(E)$ was taken from the experimental data compilation on hydrogen stopping powers in different materials [And77]. The stopping powers can be

Parameter	Value
A_0	2.652
A_1	3.0
A_2	1920.0
A_3	2000.0
A_4	0.0223

Table 4.6: Parameters for the stopping power of hydrogen in oxygen. The functional form of $STP(E)$ is given by Equations 4.9 and 4.10.

parametrized for different projectile energies. Below 10 keV,

$$STP(E) = A_0\sqrt{E} \tag{4.9}$$

In the energy region 10 keV to 1 MeV,

$$\begin{aligned} S_{low}(E) &= A_1 E^{0.45} \\ S_{high}(E) &= \frac{A_2}{E}\log(1.0 + \frac{A_3}{E} + A_4 E) \\ STP(E) &= \left(\frac{1}{S_{low}} + \frac{1}{S_{high}}\right)^{-1} \end{aligned} \tag{4.10}$$

The coefficients A_i for different elements are given in [And77]. In case of propagation of deuterons in heavy water, the material defining the stopping power is oxygen, as the beam mostly collide with oxygen atoms. The parameters for oxygen are given in Table 4.6.

For calculations of $STP(E)$ for the deuteron beam, the energy E should be 1/2 of that for hydrogen. In case if the target is composed of a mixture of elements of comparable Z, the stopping power calculations should take into account relative weights of the components, resulting in expression

$$STP(E)_{total} = \sum_i w_i STP(E)_i, \tag{4.11}$$

where w_i is the relative weight of one component, and $STP(E)_i$ is the stopping power for that element.

The energy dependence of the total cross section for the reaction was taken from the ^{2}H(d,γ)^{4}He to ^{2}H(d,p)^{3}H low energy branching ratio measurements, described in [Wil85], and usage of know energy dependence for the ^{2}H(d,p)^{3}H reaction.

The thick target analysis showed that 90% of the total yield is produced in E_d=115–52 keV range. The effective energy, corresponding to half of the total yield was found to be E_d=92 keV, or $< E_d >_{c.m.}$= 46 keV.

To compare the observed angular distributions and the results of the transition matrix element analysis of our data with the calculated TMEs and analyzing powers, the theoretical values were obtained for the effective energy, $< E_d >_{c.m.}$.

Chapter 5

TME Analysis

In the Section 3.4 we have discussed the algorithm for the extraction of the TME amplitudes and relative phases from the angular distributions of the polarization observables. Here we will present the actual data analysis.

As was noted in the Section 3.3, we considered three TMEs in the analysis: (E2, $^5s_2$), (E1, $^3p_1$), and (M2, $^3p_2$).

The TME analysis of the previous data on the $^2H(\vec{d},\gamma)^4He$ reaction at low energies included these three matrix elements and resulted in three equally probable solutions [Kra92]. Our goal was to improve the TME fit at low energies. The data at E_d=80 keV provided the differential cross section, A_y, and A_{yy} analyzing powers. The first step in our matrix element analysis was to perform the TME fit on that data to check that our new analysis code would provide the same solutions for the matrix elements. And indeed, depending on the initial amplitudes and phases, the minimization routine provided three solutions with similar values of the reduced χ^2, $\chi^2{}_\nu$, which is the total χ^2, divided by the number of degrees of freedom. The latter

Transition	Multipolarity	Fit 1		Fit 2	
	$p\mathcal{L}$	Strength,%	Phase,°	Strength,%	Phase,°
$^5s_2$	E2	28±17	0.0	12±22	0.0
$^3p_1$	E1	60±21	-145±13	11±4	-62±103
$^3p_2$	M2	12±4	-136±307	77±32	-60±58

Table 5.1: Results of TMEFIT for E_d=80 keV.

one is the difference of the total number of data points and the number of free parameters of the fit (three amplitudes and two phases in our case). Within the error bars our solutions reproduced the ones found previously, showing identical angular dependence for the polarization observables. The first fit with $\chi^2{}_\nu$ of 0.33 had similar amplitudes for all of the waves, E2 (26%), E1 (31%), and M2 (42%). The second solution, $\chi^2{}_\nu$=0.23, had dominant E1 component (61%) with strong E2 contribution (25%). The third fit, $\chi^2{}_\nu$=0.25, contained mostly M2 (72%), and similar E2 (15%) and E1 (12%) amplitudes.

Inclusion of our new data points for T_{20} in the 80-keV data set resulted in only two equally probable solutions. The first one was very close to the second solution of the previous analysis: dominating E1 (61%) amplitude, with 25% of E2 and 13 % of M2 ($\chi^2{}_\nu$=0.19). The second fit was similar to the solution "three" of the previous analysis, with dominant M2 (77%) and equally small E2 and E1 components ($\chi^2{}_\nu$=0.21). Unfortunately, lack of data points at the backward angles did not allow us to draw a definite conclusion about the TME amplitudes and phases.

Most of our data were taken at the beam energy of 115 keV. The transition matrix element analysis was performed in two ways: using only the new data for $A_y(\theta)$ and $T_{20}(\theta)$, and adding the differential cross section data from [Kra92] to the data set. The results of the two fits did not differ significantly. The data set that

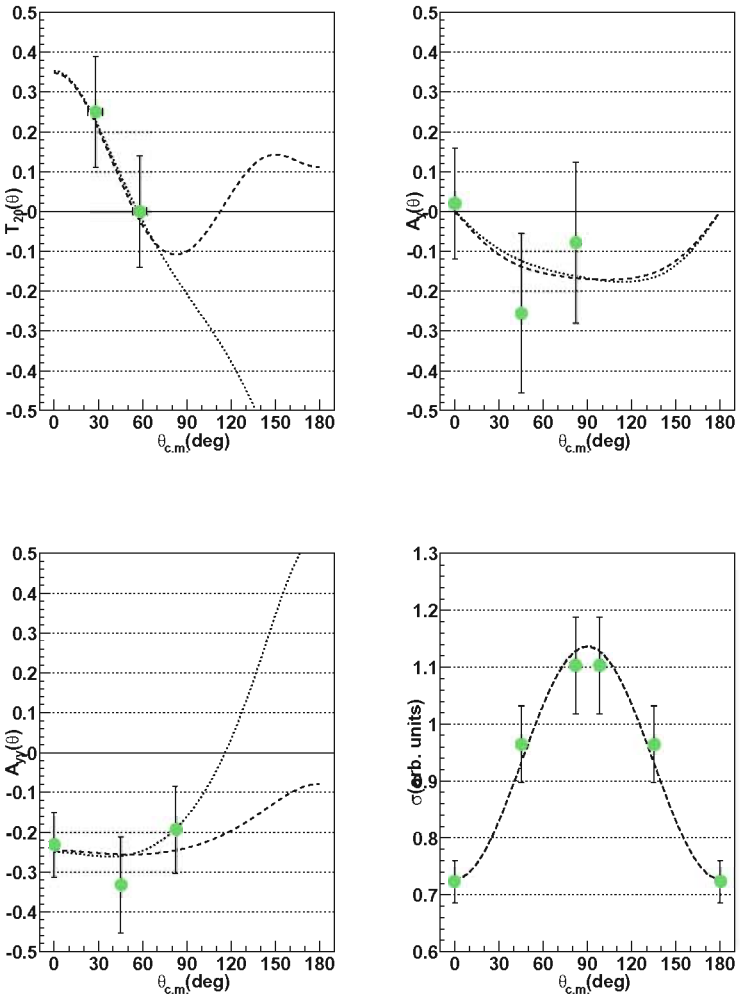

Figure 5.1: Data points and the TMEFIT results for E_d=80keV. The differential cross section, $A_y(\theta)$ and $A_{yy}(\theta)$ are from previous experiment [Kra92]. Inclusion of $T_{20}(\theta)$ data resulted in only two solutions.

Transition	Multipolarity	Fit	
	$p\mathcal{L}$	Strength,%	Phase,°
$^5s_2$	E2	55±8	0.0
$^3p_1$	E1	29±6	77±3
$^3p_2$	M2	16±3	44±8

Table 5.2: Results of TMEFIT for E_d=115 keV.

did not include the differential cross section had bigger errors on the TME amplitude values (about 20% of the total capture strength). The final fit had dominating E2 (55%) component, 29% E1 strength, and 16% of M2 amplitude. The results of the matrix elements analysis are given in Table 5.2 and Figure 5.2.

A search for more solutions was performed by changing the initial values of various parameters. For the amplitudes, the strength of one transition was varied with 20% steps, while all the other amplitudes were held unchanged. For the relative phases, a similar search was performed with 30° steps. The two solutions for E_d=80 keV and one solution for E_d=115 keV described above were the only fits with ${\chi^2}_\nu$ close to unity. For E_d=115 keV the optimal fit produced ${\chi^2}_\nu = 1.2$, while the next "best" solutions were characterized by ${\chi^2}_\nu$ values of 8.8 and 17.3. The results of this search lead to a conclusion that the found optimal fit was a unique solution.

We also investigated the possibilitiy of including different sets of matrix elements to accommodate our data. Exclusion of the p-waves (E1 or M2, or both) did not produce satisfactory fits. Inclusion of a d-wave ($^1d_2$ E2 transition being the most logical one, dominating at the energies above 1 MeV) resulted in solutions with a negligibly small $^1d_2$ component (below 3% of the total strength) and the same angular dependence for the analyzing powers. This showed that our choice of the matrix elements included in the analysis provides an adequate representation of the reaction

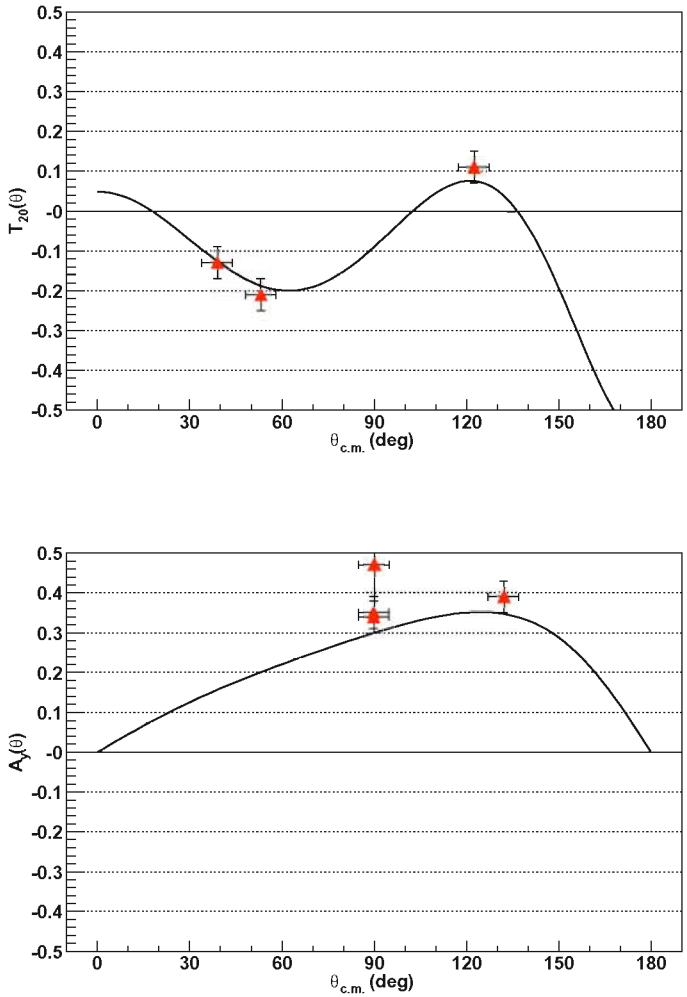

Figure 5.2: Data points and the TMEFIT results for E_d=115keV. The analysis produced a unique solution for the transition matrix elements.

at low energies.

Chapter 6

Results and Discussion

There are several models that have been used to describe the ^{2}H($\vec{d}, \gamma$)^{4}He reaction. In this chapter we will briefly discuss the direct capture model and the resonating group model.

6.1 Direct Capture Model

In direct capture model the ^{2}H(d, γ)^{4}He reaction is described as a one-step process. The reacting deuterons are treated as point-like. During the transition to the bound state they do not break up, and the ^{4}He ground state ($J^\pi = 0^+$) is considered as a system of two bound deuterons. The alpha-particle ground state can be either the S-state (with L=0, S=0), or the D-state (L=2, S=2), L referring to the relative orbital angular momentum, and S being the total spin of the two deuterons. The electromagnetic transitions from the continuum states to the bound state can be described via the transition matrix elements that have been discussed in Section 3.3.

The direct capture calculation requires the evaluation of the radial matrix elements in form of

$$\langle u_r | \mathrm{T}_L | \chi \rangle, \tag{6.1}$$

where u_r is the radial wave function of the ^{4}He ground state, and χ is the continuum two-deuteron wave function [Tos86]. The transition operators T_L are the sums of all nucleons one-body electric and magnetic transition operators, corresponding to transitions of multipolarity EL and ML. At low energies the calculations typically consider only the electric quadrupole transition (E2), and the corresponding operator for this case can be written in the long-wavelength approximation as

$$Q_{E2} = \varepsilon r^2, \tag{6.2}$$

where ε is the E2 effective charge of the two deuterons.

The alpha-particle ground state wave function is generated by solving an eigenvalue problem with the Wood-Saxon potential,

$$V(r) = V_c(r) + V_n(r), \tag{6.3}$$

where $V_c(r)$ is the Coulomb potential and $V_n(r)$ is the real central potential in the form:

$$V_n(r) = \frac{V_n}{1 + \exp(\frac{r - r_0}{a_0})} \tag{6.4}$$

The potential strength V_n is adjusted to reproduce the experimental binding energy of ^{4}He. The potential radius r_0 and the diffuseness a_0 parameters are set to the "nominal" values, to be consistent with two-body interaction models. The alpha-particle ground state is considered as a superposition of $^1\mathrm{S}_0$ and $^5\mathrm{D}_0$ states. The Wood-Saxon parameters for the two states are different. The final wave function is calculated then as a sum of S- and D-state wave functions, normalized accordingly.

Asymptotically the radial wave functions can written as

$$u_{rL} \rightarrow -N_L i^L h_L(i\alpha r), \tag{6.5}$$

where N_L is the normalization factor, and h_L is a spherical Hankel function of the first kind, with the parameter α corresponding to the separation of two deuterons from ^{4}He. The ratio N_2/N_0 is set to reproduce the adopted asymptotic D-to-S ratio.

The scattering state wave functions can be described by distorted waves, derived from the Coulomb and the nuclear optical model potential that is written as a sum of real and complex potentials in Wood-Saxon form. However it was found that at energies less than 20 MeV the depths of the imaginary potentials are very small, [Chw72]. Therefore the nuclear potential can be considered purely real, with the parameters (different sets of depth, radius and diffuseness for different scattering state partial waves) adjusted to reproduce the experimental data. The studies showed that the phase shifts obtained from a resonating group model calculations [Chw72] and potential model analysis [Blü87] provide consistent results.

The simple direct capture model can be modified and refined by including several electro-magnetic transition operators, choosing different nuclear potential forms and different asymptotic D-to-S ratios, including the deuteron D-state effects. Unfortunately, all the models assumed that at low energies the reaction is dominated by the E2 capture to the D-state.

As has been mentioned in Chapter 1, the early cross section measurements were in the agreement with the simple direct capture model predictions, but the measurements of analyzing powers showed, based on a TME analysis that, below E_d= 15 MeV, significant non-E2 components were present. Microscopic calculations, utilizing realistic nucleon-nucleon interactions in both the scattering and the bound states,

were shown to provide a description of the reaction, consistent with many experimentally observed features. Below we will discuss one of the microscopic calculations, the refined resonating group model.

6.2 Resonating Group Model

The resonating group model (RGM) is one of the most successful methods of describing few-body systems. The idea of the model came from molecular physics [Whe37], where it was developed to describe a resonant jump of a group of electrons from one atom to another. The relative wave function has to be determined from known wave functions of the fragments and interactions between and within the fragments. This leads to a multi-channel calculation with coupled channels, which can be technically challenging. Different approaches in calculating the relative wave functions and many-body integrals characterize the different flavors of the RGM. Below we will present some details of the Refined Resonating Group Model, which was used in comparison of our data to calculations. The in-depth description of the model can be found in [Hac73] and [Hof86].

All of the components of the scattering system interact via the Coulomb and the short ranged nuclear force. The nucleon-nucleon potential can be a realistic NN potential such as the Argonne AV18 potential, and the 3N terms (e.g. Urbana IX) can be easily added as well. The wave functions in the model represent six two-fragment channels: p-^{3}H, n-^{3}He, and ^{2}H-^{2}H, as well as the singlet deuteron $\bar{d}$-^{2}H, $\bar{d} - \bar{d}$, and $(nn) - (pp)$ components. The last three channels approximate the three- and four-body breakup channels that cannot in practice be treated within the RGM. The alpha-particle is considered as a combination of four clusters (four nucleons) to

allow for the internal angular momenta of ^{3}He, ^{3}H, and ^{2}H. The scattering states have s-, p-, and d-wave contributions, which are known to be enough to reproduce the experimental data at low energies.

The total wave function can be written as

$$\psi_m = \mathcal{A} \sum_n \psi_{ch}^n \psi_{rel}^{mn}, \tag{6.6}$$

where m indicates the boundary conditions, $\mathcal{A}$ denotes the antisymmetriser (to assure the proper symmetry of the total wave function),and n runs over all the channels, open, closed, and "distortion channels", describing the distortion of the fragments in the interaction region.

The internal wave function ψ_{ch} describes the coupling of angular momenta of the fragments with wave functions phi_i:

$$\psi_{ch} = \left[\frac{Y_l(\hat{\boldsymbol{R}}_{rel})}{R_{rel}} [\phi_1^{J_1} \phi_2^{J_2}]^{S_c} \right]^J, \tag{6.7}$$

where the square brackets designate the angular momenta coupling of the fragments $\phi_i^{J_i}$ to channel spin S_c, and the coupling of the orbital angular momentum l and the channel spin S_c to the total angular momentum J.

The individual fragment wave functions consist of spatial and spin-isospin components, and may contain an arbitrary number of clusters. The term "cluster" here denotes a group of particles without internal orbital angular momenta, i.e. in nuclear physics a cluster can consist at the most of 4 nucleons, two protons and two neutrons with opposite spin projections (which fill the $1s_{1/2}$ shell). The spatial part can be divided into internal and relative functions. The internal functions characterize the interaction within a cluster (e.g. a bound state of two nucleons: a deuteron). A function for a cluster a with n_a nucleons in it can be expanded as a sum of Gaussian

functions:

$$\phi_{int,a} = \exp\left(-\frac{\beta_a}{n_a}\sum_{i,j}(\boldsymbol{r}_i - \boldsymbol{r}_j)^2\right), \tag{6.8}$$

where $\boldsymbol{r}_i$ and $\boldsymbol{r}_j$ are the coordinates of the nucleons.

The relative functions, describing interaction of the clusters, in addition to Gaussians have solid spherical harmonics of various angular momenta:

$$\phi_{rell} = \exp(-\gamma s^2)\mathcal{Y}_l(\boldsymbol{s}), \tag{6.9}$$

where $\mathbf{s}$ denotes the cluster coordinates in Jacobian form and $\mathcal{Y}_l = x^l Y_{lm}(\hat{x})$ is a solid spherical harmonic. The width parameters β and γ of the Gaussians in the spatial wave functions are found using the Ritz variational principle.

The relative motion wave function is expressed as

$$\psi_{rel}^{mn}(R_{rel}) = \delta_{mn}F_m(R_{rel}) + a_{mn}\tilde{G}_n(R_{rel}) + \sum_{\nu} b_{mn\nu}\chi_{n\nu}(R_{rel}), \tag{6.10}$$

where R_{rel} is the relative coordinate between the centers of mass of the two fragments, the functions F_m and $\tilde{G}_n$ are regular and regularized irregular Coulomb functions, and $\chi_{n\nu}$ are square integrable functions of Gaussian type. The coefficients a_{mn} and $b_{mn\nu}$ can be found by utilizing the Kohn-Hulthén variational procedure on the channel wave function ψ_m.

The calculation of the matrix elements of the Hamiltonian, nucleon-nucleon potential, or electromagnetic transitions, involves taking a large number of integrals of the spatial part of the clusters, consisting of a superposition of multidimensional Gaussian functions and solid harmonics. The scale of the calculation requires the use of computers, but the procedure itself can be applied to a wide variety of operators, and with sufficient computing power can be used to describe an arbitrary number of clusters.

It should be stressed that the inclusion of multiple coupled channels is one of the key features of the calculation. It has been shown in previous, less detailed microscopic multi-channel resonating group model calculations [Wac87], that the presence of E1, M1, and M2 radiation can only be explained by considering the coupling to the p-^{3}H and n-^{3}He channels.

Moreover, the equal treatment of different cluster configurations makes is possible to calculate various reactions at the same time. For example, for the A=4 system, the ^{2}H+^{2}H, p+^{3}H, and n+^{3}He reactions can be considered within one model, to provide radiative capture, photo breakup, charged-particle and neutron capture reaction observables.

6.3 Comparison of Data with Models

The refined resonating group model calculations for the ^{4}He system were performed by H. R. Hofmann and M. Trini, [Hof03]. The calculations produced transition matrix elements for E2, E1, and M2 electromagnetic transitions, as well as the angular distributions and the energy dependence of analyzing powers.

Our observed analyzing powers and the the TMEs obtained via the transition matrix analysis of our data were compared to the calculations at the energy corresponding to the effective energy for the deuterons stopped in the heavy-water target (for the detailed discussion of the effective energy see Chapter 4). For E_d=115 keV deuterons the effective energy for stopping in a D_2O target is 46 keV in the center of mass.

The summary of the results of the TME analysis and the RRGM calculations are given in Table 6.1. The calculations were also performed with two extra E2 transitions

Transition	Multipolarity	TME Fit		RRGM	
	$p\mathcal{L}$	Strength,%	Phase,°	Strength,%	Phase,°
$^5S_2$	E2	55±8	0.0	59	122 (0)
$^3p_1$	E1	29±6	77±3	26	-61 (-183)
$^3p_2$	M2	16±3	44±8	11	82 (-40)

Table 6.1: Results of the TME fit analysis and RRGM calculations for $< E_d >_{cm}$=46 keV. The rest of the calculated capture strength (4%) is due to d-wave E2 capture, which was not included in the TME fit. The calculated phases, shifted by -122° for comparison with the TME analysis are shown in parentheses.

included: $^5d_2$ and $^1d_2$ capture waves. The amplitude of the $^5d_2$ TME was found to be less than 0.01% of the total capture strength, and the amplitude of the $^1d_2$ TME was less than 3%; these results are consistent with the results of our TME analysis, where the presence of E2 d-waves was found to be negligible.

The data points, adjusted for finite geometry (see Table 4.5), along with angular distributions of T_{20} and A_y analyzing powers determined by the TME analysis of the data and the RRGM calculations are presented in Figures 6.1 and 6.2.

The results of the RRGM calculation are in very good agreement with the relative amplitude strengths obtained from the transition matrix element analysis of our data. The calculated phases do differ from the results of the TME fit, but the general shape of analyzing power angular distributions is reproduced. The signs of the relative phases, however, do not agree with our analysis. The negative signs p-wave relative phases results in negative values of the vector analyzing power A_y (as a remark, if the signs of the calculated phases are changed to opposite, and 90° are subtracted from the E1 phase, the A_y values would become positive, and both, A_y and T_{20} look very close to the TMEFIT results; this might indicate that a phase factor might be one of explanations of the discrepancy). The full calculation is still being developed and the reasons for the discrepancy in the relative phase values are currently under

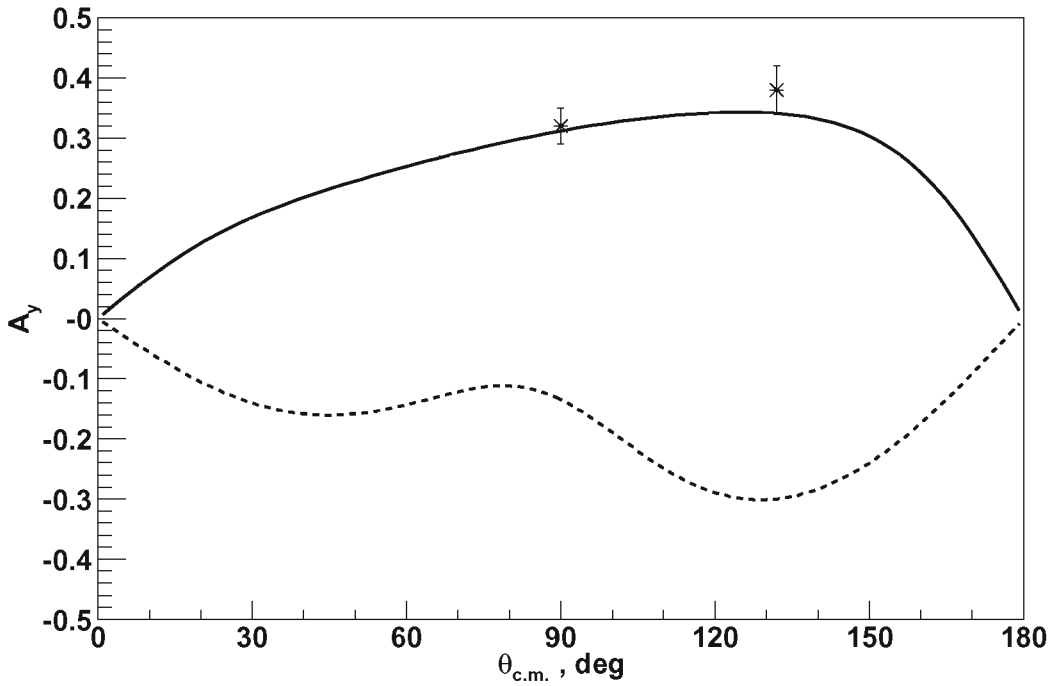

Figure 6.1: Measured vector analyzing power $A_y(\theta)$, corrected for finite geometry, the TMEFIT results (solid curve) , and the refined resonating group calculation results (dashed curve) for $< E_d >_{cm}$=46keV.

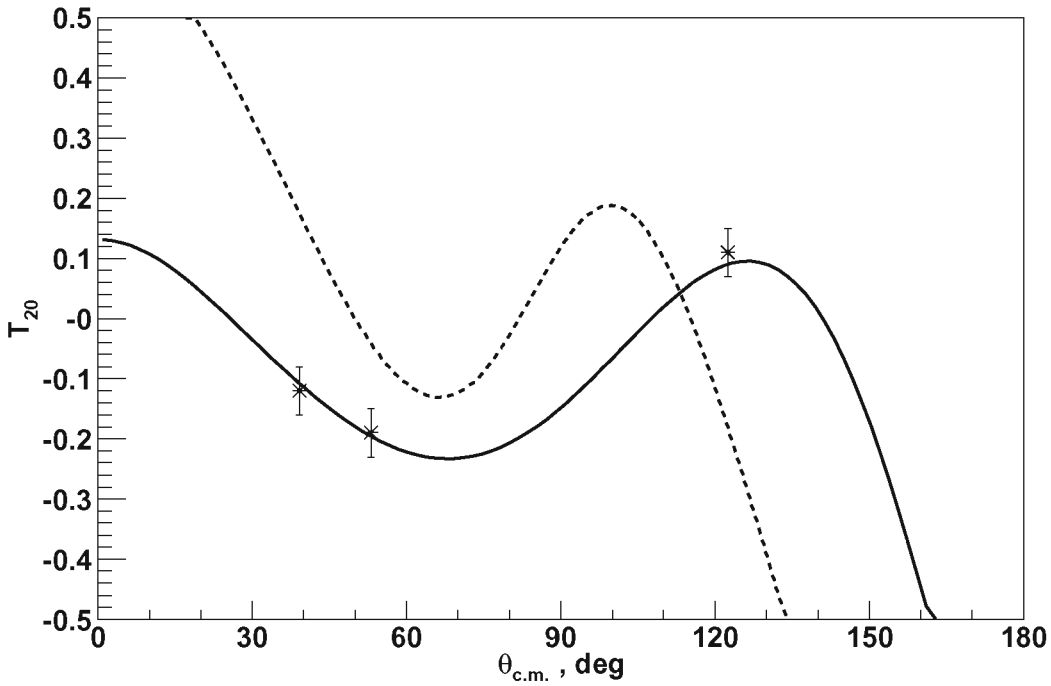

Figure 6.2: Measured tensor analyzing power $T_{20}(\theta)$, corrected for finite geometry, the TMEFIT results (solid curve), and the refined resonating group calculation results (dashed curve) for $< E_d >_{cm}$=46keV.

investigation, [Hof03].

The impact of these results on the extrapolated value of the astrophysical S-factor will be discussed in the next chapter.

Chapter 7

Conclusion

The improved design of the target chamber and use of ice target permitted high quality measurements of tensor analyzing power T_{20} and vector analyzing power A_y angular distributions at E_d=115 keV.

The quality of the data resulted in an unambiguous transition matrix element analysis; the TME fit of the data produced a unique solution, other local minima posessing the χ^2 per degree of freedom values factor 8–10 higher than the optimal fit . The analysis included three complex terms: $^5s_2$ (E2), $^3p_1$ (E1), and $^3p_2$ (M2) transition matrix elements. It was found that while the s-wave E2 capture is dominant, producing 55% of the total capture strength, the p-wave capture is significant (45%), with contributions of E1 and M2 transitions being 29% and 16% of the total capture strength respectively.

The experimental data and the TME analysis results were compared to the refined resonating group model calculations [Hof03]. The calculated relative amplitudes of the transition matrix elements were found to be in good agreement with the ones

produced by the TME analysis. This model implies that the observed E1 and M2 p-wave capture strength arises from the coupling of the p-T and n-^{3}He channels to the d-d channel.

The experimental observation of significant p-wave capture strength at low energies and the theoretical confirmation of this phenomenon will lead to modification of the adopted extrapolated astrophysical S-factor value for the ^{2}H$(\vec{d},\gamma)^4$He reaction. The previous studies, even based on microscopic calculations such as [Ass87], included only E2 transitions. The resulting S-factor curve had a slightly negative slope at low energies. But the inclusion of the p-wave capture, which was made possible through the coupling of multiple channels, changes the slope to positive, lowering the extrapolated value of the S-factor. On Figure 7.1 the pure E2 calculation (solid line) is shown along with the RRGM results (the lower solid curve at energies below 60 keV). The pure E2 calculation was adjusted to fit the experimental values of the cross section. If we scale the RRGM up by factor of 1.6 (the dashed curve) to be more consistent with the data in the energy region of $E_{dc.m.}$=40–60 keV,the extrapolated value of the S-factor would be 2 times lower than the previously calculated one.

More complete refined resonating group calculations, including the distortion channels and more realistic potentials, are under way. The inclusion of the distortion channels would better describe the changes of the wave functions in the interaction region, and should produce a more attractive potential, and therefore scale up the value of the S-factor, making it more consistent with the experimental data.

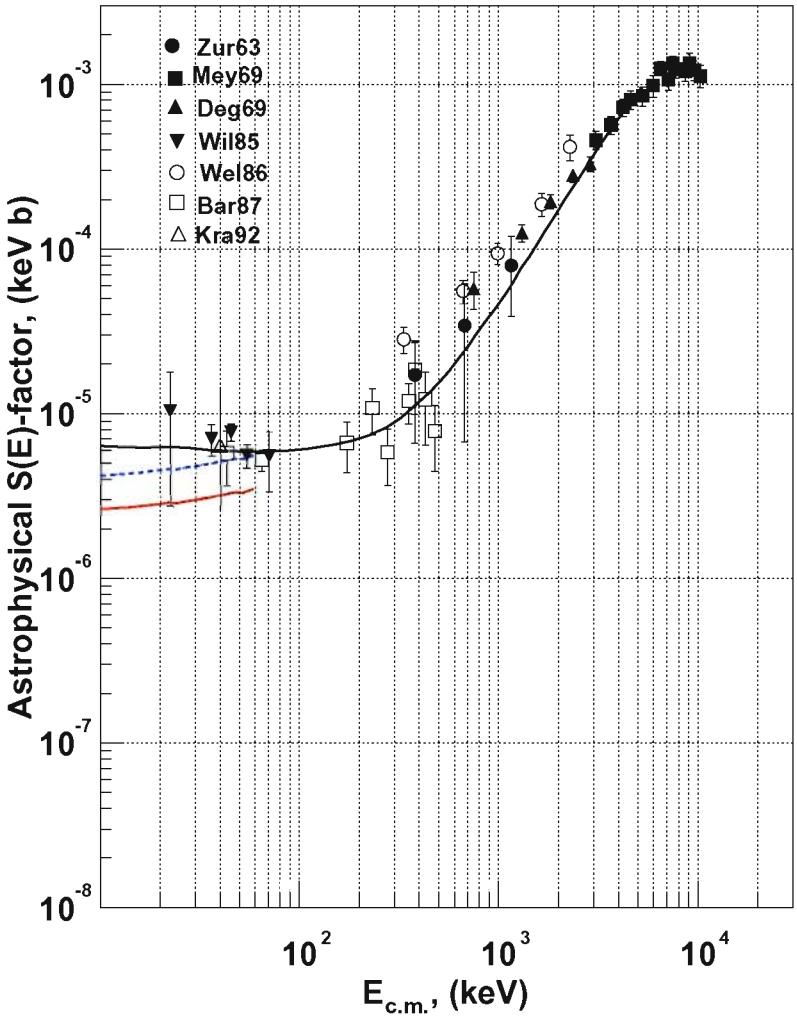

Figure 7.1: Energy dependence of ^{2}H(d,γ)^{4}He astrophysical S-factor. The experimental data are from [Zur63], [Mey69], [Deg92], [Wil85], [Wel86], [Bar87], and [Kra92]. The pure E2 semimicroscopic calculation (solid curve) and the refined resonating group calculation (the lower solid line for energies below 60 keV) are shown. To directly compare the two, the RRGM calculation is scaled up by factor of 1.6. Inclusion of the p-wave capture changes the slope of the S-factor at low energies.

Bibliography

[And77] H. H. Anderson and J. F. Ziegles. *Hydrogen Stopping Powers and Ranges in All Elements.* Pergammon, New York, 1977.

[Arr88] A. Arriaga, A. M. Eiro, F. D. Santos, and J. E. Ribeiro. Phys. Rev. C, **37**(1988) 2312–2319.

[Arr91] A. Arriaga, V. R. Pandharipande, and R. Schiavilla. Phys. Rev. C, **43**(1991) 983–991.

[Ass87] H. J. Assenbaum and K. Langanke. Phys. Rev. C, **36**(1987) 17–20.

[Bal92] M. J. Balbes. Ph.D. thesis, Duke University, 1992.

[Bar71] H. H. Barschall, editor. *Polarization Phenomena in Nuclear Reactions*, page xxv. University of Wisconson Press, Madison, Wisconsin, 1971.

[Bar87] C. A. Barnes et al. Phys. Lett. B, **197**(1987) 315–319.

[Bed00] P. F. Bedaque, H.-W. Hammer, and U. van Kolck. Nucl. Phys., **A676**(2000) 357–370.

[Bev69] P. R. Bevington. *Data Reduction and Error Analysis for the Physical Sciences*, page 60. McGraw-Hill Book Company, New York, 1969.

[Blü87] G. Blüge, H. J. Assenbaum, and K. Langanke. Phys. Rev. C, **36**(1987) 21–26.

[Bre31] G. Breit and I. I. Rabi. Phys. Rev., **38**(1931) 2082–2083.

[Bro90] R. E. Brown and N. Jarmie. Phys. Rev. C, **41**(1990) 1391–1400.

[Can00] L. Canton and W. Schadow. Phys. Rev. C, **62**(2000) 044005.

[Chw72] F. S. Chwieroth, Y. C. Tang, and D. R. Thompson. nphy, **A189**(1972).

[Cle90] T. B. Clegg. Rev. Sci. Instr., **61**(1990) 385.

[Coo79] S. A. Coon et al. Nucl. Phys., **A317**(1979) 242.

[Deg92] A. Degré. Ph.D. thesis, Université de Strasbourg, 1992.

[Edm74] A. R. Edmonds. *Angular Momentrum In Quantum Mechanics.* Princeton University Press, Princeton, New Jersey, 1974.

[Fer65] A. J. Ferguseon. *Angular Correlation Methods in Gamma-Ray Spectroscopy.* John Wiley & Sons, New York, 1965.

[Fle94] K. A. Fletcher et al. Phys. Rev. C, **49**(1994) 2305–2310.

[Hac73] H. H. Hackenbroich. page 706, Bologna, 1973. Editrice Compositori. Proceedings of the International Symposium on Present status and novel developments in the nuclear many-body-problem.

[Hof86] H. M. Hofmann. *Resonating Group Calculations in Light Nuclear Systems.* In L. S. Ferreira, A. C. Fonesca, and L. Streit, editors, *Lecture Notes in Physics*, volume 273, page 243, Berlin, 1986. Springer. Proceedings of Models and Methods in Few-Body Physics.

[Hof97] H. M. Hofmann and G. M. Hale. Nucl. Phys., **A613**(1997) 69–106.

[Hof02] H. M. Hofmann and G. M. Hale. nucl-th/0211008, (2002).

[Hof03] H. M. Hofmann and M. Trini. Private communications, (2003).

[Jam71] F. James and M. Roos. *MINUIT.* CERN Computer Centre Program Library, 1971.

[Kad86] H. Kadana, T. Kaneko, and Y. C. Tang. Phys. Rev. C, **34**(1986) 22–31.

[Kap01] M. Kaplinghat and M. .S Turner. Phys. Rev. Lett., **86**(2001) 385–388.

[Koi87] Y. Koike and J. Haidenbauer. Nucl. Phys., **A463**(1987).

[Kra92] L. H. Kramer. Ph.D. thesis, Duke University, 1992.

[Kra93] L. H. Kramer et al. Phys. Lett. B, **304**(1993) 208–213.

[Lan88] J. L. Langenbrunner, G. Feldman, H. R. Weller, D. R. Tilley, B. Wachter, T. Mertelmeier, and H. M. Hofmann. Phys. Rev. C, **38**(1988) 565.

[Lan89] J. L. Langenbrunner. Ph.D. thesis, Duke University, 1989.

[Mel86] S. Mellema, T. R. Wang, and W. Haeberli. Phys. Rev. C, **34**(1986) 2043–2048.

[Mey69] W. E. Meyerhof, W. Feldman, S. Gilbert, and W. O'Connell. Nucl. Phys., **A131**(1969) 489.

[Nog02] A. Nogga, H. Kamada, W. Glöckle, and B. R. Barrett. Phys. Rev. C, **65**(2002) 054003.

[Phi87] R. J. Philpott. NIM, **A259**(1987) 317–323.

[Pie87] J. Piekarewicz and S. E. Koonin. Phys. Rev. C, **36**(1987) 875–878.

[Pud97] B. S. Pudliner et al. Phys. Rev. C, **56**(1997) 1720.

[Sey79] R. G. Seyler and H. R. Weller. Phys. Rev. C, **20**(1979) 453.

[Tag92] Y. Tagishi et al. Phys. Rev. C, **46**(1992) 1155–1158.

[Tos86] J. A. Tostevin. Phys. Rev. C, **34**(1986) 1497–1500.

[Wac87] B. Wachter, T. Mertelmeier, and H. M. Hofmann. Phys. Lett. B, **200**(1987) 246–250.

[Wel84] H. R. Weller, P. Colby, N. R. Roberson, and D. R. Tilley. Phys. Rev. Lett., **53**(1984) 1325–1328.

[Wel86] H. R. Weller, P. Colby, J. L. Langenbrunner, Z. D. Huang, D. R. Tilley, F. D. Santos, A. Arriaga, and A. M. Eiro. Phys. Rev. C, **34**(1986) 32–37.

[Whe37] J. A. Wheeler. Phys. Rev., **52**(1937) 1083.

[Whi93] R. M. Whitton, H. R. Weller, E. Hayward, W. R. Dodge, and S. E. Kuhn. Phys. Rev. C, **48**(1993) 2355–2365.

[Wil69] D. H. Wilkinson, editor. *Isospin in Nuclear Physics*, page 185. North Holland, Amsterdam, 1969.

[Wil85] F. J. III Wilkinson and F. E. Cecil. Phys. Rev. C, **31**(1985) 2036–2040.

[Wir95] R. B. Wiringa, V. G. J. Stoks, and R. Schiavilla. Phys. Rev. C, **51**(1995) 38.

[Wur97] J. Wurzer and H. M. Hofmann. Phys. Rev. C, **55**(1997) 688–698.

[Zur63] R. W. Zurmühle, W. E. Stephens, and H. H. Staub. Phys. Rev., **132**(1963) 489.

Biography

Konstantin Sabourov

Personal

- Born in 1975, Russian Federation, Soviet Union

Education

- B.S. Physics, Moscow Institute of Physics and Technology, Dolgoprudny, Russia, 1996
- M.A. Physics, Duke University, Durham, NC, 2001

Positions

- Teaching Assistant, Duke University, 1996-1998
- Research Assistant, Duke University, TUNL, 1998-2003

Publications

"Parity Measurements of Nuclear Levels Using a Free-Electron-Laser Generated γ-Ray Beam," (N. Pietralla and Z. Berant, M. W. Ahmed, J. H. Kelley, S. O. Nelson, R. Prior, K. Sabourov, A. P. Tonchev, and H. R. Weller, V. N. Litvinenko, S. Hartman, F. F. Mikhailov, I. V. Pinayev, and G. Swift), Phys. Rev. Lett, **88**, 012502 (2002).

"Identification of the $J^{\pi} = 1^{-}$ two-phonon state of ^{88}Sr," (N. Pietralla, V. N. Litvinenko, S. Hartman, F. F. Mikhailov, I. V. Pinayev, G. Swift, M. W. Ahmed, J. H. Kelley, S. O. Nelson, R. Prior, K. Sabourov, A. P. Tonchev, and H. R. Weller), Phys. Rev. C **65**, 044088 (2002).

"$^3H(\vec{p},\gamma)^4He$ reaction below E_p=80 keV," (R. S. Canon, S. O. Nelson, K. Sabourov, E. Wulf, H. R. Weller, R. M. Prior, M. Spraker, J. H. Kelley, and D. R. Tilley), Phys. Rev. C **65** , 044008 (2002).

"Ratio of S-factors for (p,γ) reactions on ^{12}C and ^{13}C at astrophysically relevant energies," (C. D. Nesaraja, C. R. Brune, B. T. Crowley, J. H. Kelley, S. O. Nelson, R. M. Prior, K. Sabourov, D. R. Tilley, A. Tonchev, and H. R. Weller), Phys. Rev. C **64** , 065804 (2001).

"First measurement of the near-threshold $^2H(\vec{\gamma},n)p$ analyzing power using a free-electron laser based γ-ray source," (E. C. Schreiber, R. S. Canon, B. T. Crowley, C. R. Howell, J. H. Kelley, V. N. Litvinenko, S. O. Nelson, S. H. Park, I. V. Pinayev, R. M. Prior, K. Sabourov, M. Spraker, W. Tornow, Y. Wu, E. A. Wulf, and H. R. Weller), Phys. Rev. C **61** , 061604 (2000).

"Spin parity of the 7.478 MeV state of ^{10}B and the S-factor of the $^9Be(\vec{p},\gamma_0)^{10}B$ reaction," (S. J. Gaff, R. S. Canon, J. H. Kelley, S. O. Nelson, K. Sabourov, E. C. Schreiber, D. R. Tilley, H. R. Weller, and E. A. Wulf), Phys. Rev. C **59**, 3425-3428 (1999).

"Exclusive electroproduction of ϕ-mesons at 4.2 GeV," (K. Lukashin et al. (The CLAS Collaboration)), Phys. Rev. C **63** , 065205 (2001).

"Electroproduction of the $\Lambda(1520)$ hyperon," (S. P. Barrow et al. (The CLAS Collaboration)), Phys. Rev. C **64** , 044601 (2001).